General Disclaimer

One or more of the Following Statements may affect this Document

- This document has been reproduced from the best copy furnished by the organizational source. It is being released in the interest of making available as much information as possible.

- This document may contain data, which exceeds the sheet parameters. It was furnished in this condition by the organizational source and is the best copy available.

- This document may contain tone-on-tone or color graphs, charts and/or pictures, which have been reproduced in black and white.

- This document is paginated as submitted by the original source.

- Portions of this document are not fully legible due to the historical nature of some of the material. However, it is the best reproduction available from the original submission.

81

MESOMETEOROLOGY PROJECT

Department of the Geophysical Sciences
The University of Chicago

DYNAMICAL ANALYSIS OF OUTFLOW FROM TORNADO-PRODUCING THUNDERSTORMS AS REVEALED BY ATS III PICTURES

by

K. Ninomiya
The University of Chicago

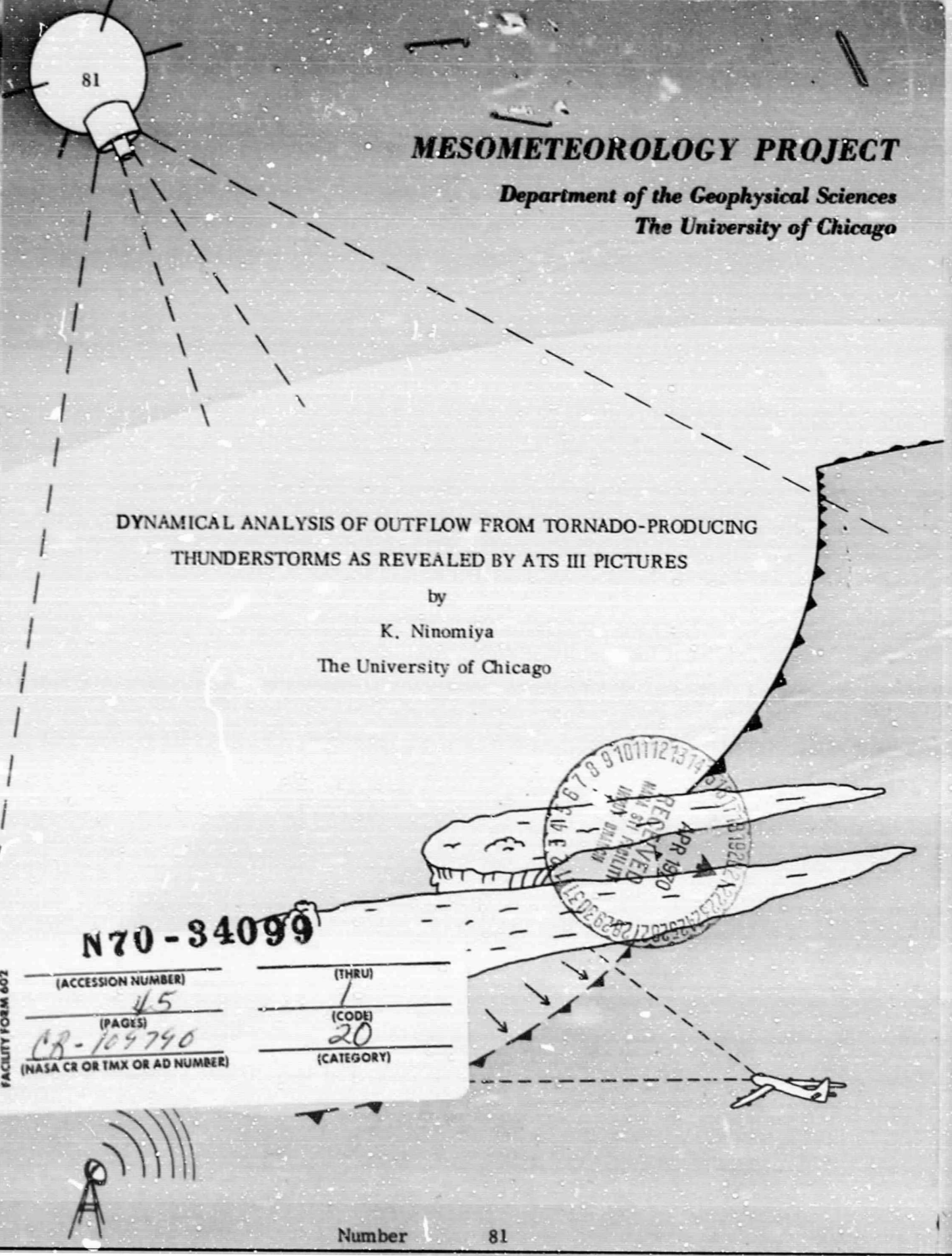

W. R. Bandeen

MESOMETEOROLOGY PROJECT --- RESEARCH PAPERS

1.* Report on the Chicago Tornado of March 4, 1961 - Rodger A. Brown and Tetsuya Fujita

2.* Index to the NSSP Surface Network - Tetsuya Fujita

3.* Outline of a Technique for Precise Rectification of Satellite Cloud Photographs - Tetsuya Fujita

4.* Horizontal Structure of Mountain Winds - Henry A. Brown

5.* An Investigation of Developmental Processes of the Wake Depression Through Excess Pressure Analysis of Nocturnal Showers - Joseph L. Goldman

6.* Precipitation in the 1960 Flagstaff Mesometeorological Network - Kenneth A. Styber

7.** On a Method of Single and Dual-Image Photogrammetry of Panoramic Aerial Photographs - Tetsuya Fujita

8. A Review of Researches on Analytical Mesometeorology - Tetsuya Fujita

9.* Meteorological Interpretations of Convective Nephsystems Appearing in TIROS Cloud Photographs - Tetsuya Fujita, Toshimitsu Ushijima, William A. Hass, and George T. Dellert, Jr.

10.* Study of the Development of Prefrontal Squall-Systems Using NSSP Network Data - Joseph L. Goldman

11. Analysis of Selected Aircraft Data from NSSP Operation, 1962 - Tetsuya Fujita

12. Study of a Long Condensation Trail Photographed by TIROS I - Toshimitsu Ushijima

13. A Technique for Precise Analysis of Satellite Data; Volume I - Photogrammetry (Published as MSL Report No. 14) - Tetsuya Fujita

14. Investigation of a Summer Jet Stream Using TIROS and Aerological Data - Kozo Ninomiya

15. Outline of a Theory and Examples for Precise Analysis of Satellite Radiation Data - Tetsuya Fujita

16. Preliminary Result of Analysis of the Cumulonimbus Cloud of April 21, 1961 - Tetsuya Fujita and James Arnold

17.* A Technique for Precise Analysis of Satellite Photographs - Tetsuya Fujita

18.* Evaluation of Limb Darkening from TIROS III Radiation Data - S.H.H. Larsen, Tetsuya Fujita, and W.L. Fletcher

19. Synoptic Interpretation of TIROS III Measurements of Infrared Radiation - Finn Pedersen and Tetsuya Fujita

20.* TIROS III Measurements of Terrestrial Radiation and Reflected and Scattered Solar Radiation - S.H.H. Larsen, Tetsuya Fujita, and W.L. Fletcher

21. On the Low-level Structure of a Squall Line - Henry A. Brown

22.* Thunderstorms and the Low-level Jet - William D. Bonner

23.* The Mesoanalysis of an Organized Convective System - Henry A. Brown

24. Preliminary Radar and Photogrammetric Study of the Illinois Tornadoes of April 17 and 22, 1963 - Joseph L. Goldman and Tetsuya Fujita

25. Use of TIROS Pictures for Studies of the Internal Structure of Tropical Storms - Tetsuya Fujita with Rectified Pictures from TIROS I Orbit 125, R/O 128 - Toshimitsu Ushijima

26. An Experiment in the Determination of Geostrophic and Isallobaric Winds from NSSP Pressure Data - William Bonner

27. Proposed Mechanism of Hook Echo Formation - Tetsuya Fujita with a Preliminary Mesosynoptic Analysis of Tornado Cyclone Case of May 26, 1963 - Tetsuya Fujita and Robbi Stuhmer

28. The Decaying Stage of Hurricane Anna of July 1961 as Portrayed by TIROS Cloud Photographs and Infrared Radiation from the Top of the Storm - Tetsuya Fujita and James Arnold

29. A Technique for Precise Analysis of Satellite Data, Volume II - Radiation Analysis, Section 6, Fixed-Position Scanning - Tetsuya Fujita

30. Evaluation of Errors in the Graphical Rectification of Satellite Photographs - Tetsuya Fujita

31. Tables of Scan Nadir and Horizontal Angles - William D. Bonner

32. A Simplified Grid Technique for Determining Scan Lines Generated by the TIROS Scanning Radiometer - James E. Arnold

33. A Study of Cumulus Clouds over the Flagstaff Research Network with the Use of U-2 Photographs - Dorothy L. Bradbury and Tetsuya Fujita

34. The Scanning Printer and Its Application to Detailed Analysis of Satellite Radiation Data - Tetsuya Fujita

35. Synoptic Study of Cold Air Outbreak over the Mediterranean using Satellite Photographs and Radiation Data - Aasmund Rabbe and Tetsuya Fujita

36. Accurate Calibration of Doppler Winds for their use in the Computation of Mesoscale Wind Fields - Tetsuya Fujita

37. Proposed Operation of Intrumented Aircraft for Research on Moisture Fronts and Wake Depressions - Tetsuya Fujita and Dorothy L. Bradbury

38. Statistical and Kinematical Properties of the Low-level Jet Stream - William D. Bonner

39. The Illinois Tornadoes of 17 and 22 April 1963 - Joseph L. Goldman

40. Resolution of the Nimbus High Resolution Infrared Radiometer - Tetsuya Fujita and William R. Bandeen

41. On the Determination of the Exchange Coefficients in Convective Clouds - Rodger A. Brown

* Out of Print
** To be published

(Continued on back cover)

SATELLITE AND MESOMETEOROLOGY RESEARCH PROJECT
Department of the Geophysical Sciences
The University of Chicago

DYNAMICAL ANALYSIS OF OUTFLOW FROM TORNADO-PRODUCING THUNDERSTORMS AS REVEALED BY ATS III PICTURES

by
K. Ninomiya
The University of Chicago

SMRP Research Paper No. 81
December 1969

The research reported in this paper was supported by the National Aeronautics and Space Administration under grant NGR 14-001-008 and the Environmental Science Services Administration under grants USESSA E-22-41-69 (G) and ESSA E-198-68 (G).

DYNAMICAL ANALYSIS OF OUTFLOW FROM TORNADO-PRODUCING THUNDERSTORMS AS REVEALED BY ATS III PICTURES[1]

by

K. Ninomiya[2]

The University of Chicago

ABSTRACT

Detailed synoptic and dynamic analyses of outflow from tornado-producing thunderstorms of April 23, 1968 were made by using conventional rawinsonde data combined with ATS III pictures. It was found that the pre-existing flow at the cirrus level over storm areas changed dramatically into outflow as the storms developed. When the storms reached their mature stage, the horizontal dimensions of the outflow increased to about 500 km. Detailed analyses of rawinsonde data inside the outflow area revealed the existence of a mid-tropospheric warm core accompanied by a significant field of convergence below the 700-mb surface.

Quantitative analysis of the thermodynamical and dynamical aspects of the outflow field showed that the outflow was induced and maintained by convective warming.

1. Introduction

In order to understand the dynamical aspects of severe local storms many researchers have tried to describe the three-dimensional wind field making use of both aerological and aircraft data (see Fujita (1963) and Newton (1963 and 1967)).

It has been pointed out that mesoscale outflow is found over developed thunderstorms. Using a Project Jetstream flight into a squall line of April 23, 1957, McLean (1961) obtained an outflow pattern in the layer between 36,000 and 40,000 ft over the thunderstorm. In the analysis of a huge cumulonimbus, Fujita and Arnold (1963) showed that the anvil

---

[1]The research reported in this paper has been supported by the National Aeronautics and Space Administration under grant NGR 14-001-008 and the Environmental Science Services Administration under grants USESSA E-22-41-69(G) and ESSA E-198-68 (G).

[2]On leave from the Meteorological Research Institute, Tokyo, Japan.

cloud grew rapidly from the echo area. By using wind data obtained by high-level observation flights, staff members of the National Severe Storms Project (1963) showed that the high level wind speed increased over the lee side of severe storms. The use of both aircraft and rawinsonde data, however, is limited for the determination of the outflow field as a function of time, because the outflow from the thunderstorms is much smaller in area and shorter in life than that of hurricanes.

Series of photographs obtained by the geosynchronous ATS satellite have been found useful in determining the cloud velocity field. In the spring of 1968, NASA and ESSA conducted the Tornado Watch Experiment. On days when severe storms were expected, ATS III took pictures at 14 minute intervals. Fujita and Bradbury (1969) determined the mass outflow from a thunderstorm complex on April 19, 1968 by computing the high clouds' displacement observed by the ATS III pictures. It is the special advantage of ATS observations that the cloud velocity field can be determined during the entire period of thunderstorm development.

In this paper, the upper level outflow from the tornado-producing thunderstorms on April 23, 1968 will be analysed both synoptically and dynamically in detail by using rawinsonde data combined with a series of ATS III pictures of the Tornado Watch Experiment. It is the purpose of the study to clarify the role of the convective warming in the dynamical process of the formation of the outflow.

2. Description of the Severe Storms Synoptic Situation of 23 April 1968

On the morning of 23 April 1968 there was a moderately developed extratropical cyclone over southwest Wisconsin with a weak trough line extending through central Illinois, western Kentucky and Tennessee. During the day, the cyclone remained nearly stationary and as the trough line moved eastward a secondary low pressure center developed. By 1800 CST this secondary low center had become intense and was located over eastern Michigan.

In the mid-troposphere a cut-off cold core (500— 400 mb) was centered south of the surface cyclone center during the morning of 23 April. As this cold core moved northeastward over the Great Lakes region, it passed over the very moist and warm lower

tropospheric air mass which was being advected ahead of the surface trough by strong southerly flow. This fits the model for a typical synoptic situation for severe storm development described by Fawbush, Miller and Starret (1951). Figure 1 shows the conditions that existed at 1200 CST. Surface isotherms and mixing ratios are shown in the figure with the 1,000 ft. winds. Also included is the movement of the cut-off cold core during the 12-hour period between 0600 CST and 1800 CST.

The remarkably unstable stratification was brought over southeastern Indiana in the early afternoon. The initial development of the thunderstorms occurred between 1100 CST and 1200 CST. The thunderstorms grew rapidly as they moved northeastward with the speed of 50—60 knots. The maximum storm activity occurred between 1400 CST and 1700 CST, and the activity of the storms continued late into the night of the 23rd.

3. High-Level Flow Obtained from Cloud Movement

Detailed analysis of the cloud displacement in the upper layers was made by tracing cloud movements from a film loop of consecutive ATS III pictures taken at 14 minute intervals. The film loop was put on a "loop movie projector" designed by Fujita and the cloud displacement between first and last picture represented the cloud motion during that interval of time. The velocity in the cloud layer was assumed to be equal to the velocity of the cloud movement. The moist layers were found from rawinsonde observations in the convective layer and also in the higher troposphere. The wind field in the higher troposphere was obtained by tracing the movements of high clouds.

The ATS III pictures and the displacement of clouds for the three stages of the thunderstorm complexes, i.e., the initial stage, the growing stage and the mature stage, are presented in Fig. 2, 3, and 4, respectively. Shown in Fig. 2a is the ATS III picture at 1100 CST. The bright cloud mass which was located in southern Indiana at this time grew explosively into a huge triangle-shaped cloud in two hours as observed in Fig. 3a. Fig. 2b shows the cloud displacement in the initial stage of the storms. No significant mesoscale difluence flow pattern or mesoscale divergence field is observed prior to and in the initial stage of the storms' development.

The velocity field of high clouds in Fig. 3b shows a remarkable change from the field

two hours earlier. The flow around the huge triangle-shaped cloud became a remarkable mesoscale difluence flow.

As several mesosystems developed successively, the high cloud sheet grew from each storm and they formed a large nephsystem as shown in Fig. 4a. This large nephsystem is considered to be a large-scale nephsystem rather than a mesoscale one because its horizontal scale is about 500 km or more. The cloud velocity field at the time corresponding to the picture in Fig. 4a is shown in Fig. 4b. A mesoscale difluence flow pattern is observed not only over each thunderstorm, but also a large-scale difluence flow pattern is observed over the whole area of mature thunderstorms.

It might be questioned whether or not the high clouds' movement does, indeed, represent the wind velocity field at a certain isobaric surface. However, a comparison of the clouds' movement with the wind velocity observed by the rawinsonde shows a strong correlation. The comparisons made at HTS and BUF for 1800 CST are shown in Fig. 5 as examples. We can see that the high clouds' movement coincides almost with the wind in the layer between 300 and 200 mb. Of course, the heights of all individual clouds are not necessarily uniform. The height difference among these clouds would be two thousand meters at most. The height difference would not make, however, serious error in the wind velocity estimation in the outflow layer because the vertical wind shear in the layer is fortunately small (see Fig. 5 and Fig. 10). Because some irregular variation in the velocity field given in Figs. 2b, 3b, and 4b is due to the height difference, in all quantitative analyses in this section, the irregularity of the wind field was eliminated by areal smoothing.

In order to describe characteristics of the outflow quantitatively, it is necessary to evaluate divergence, vorticity and deformation in the outflow layer. The evaluation of the mean divergence is made over the areas indicated in Figs. 6a and 6b, where boundary $\widehat{AB}$ and $\widehat{CD}$ are normal to the stream lines everywhere while $\widehat{BC}$ and $\widehat{DA}$ are parallel to the stream lines. The mean divergence in the area is therefore written as

$$\overline{\mathrm{div}\,\mathbf{V}} = \frac{1}{S}\oint V_n \, ds = \frac{1}{S}\left[\int_B^A V \, ds + \int_D^C V \, ds \right] \qquad (1)$$

where V_n , is the component of wind normal to the boundary, ds , the line element along the boundary and S , the dimension of the area.

Shown in Fig. 6a is the evaluation of divergence over the developing thunderstorm complex. The amount of the outflow across the downstream side boundary is $9 \times 10^6 m^2 sec^{-1}$ while that of inflow across the upstream side boundary is only $2 \times 10^6 m^2 sec^{-1}$. The mean divergence over this mesoscale area ($S = 6 \times 10^{10} m^2$) is, thus, evaluated as $12 \times 10^{-5} sec^{-1}$.

The evaluation for the mature stage is made over the relatively larger area (Fig. 6b). As the dimension of the area is $29 \times 10^{10} m^2$, the result of this evaluation should be considered as the value of the large-scale divergence field rather than that of the meso-scale field. We have $28 \times 10^6 m^2 sec^{-1}$ of the outflow across the downstream boundary against $7 \times 10^6 m^2 sec^{-1}$ of the inflow across the upstream boundary. In spite of the large area for the calculation, the magnitude of the mean divergence is as large as $7 \times 10^{-5} sec^{-1}$. The above results indicate that there was strong upward motion just below the outflow layer.

The values of divergence mentioned above are the value of mean divergence defined in the area whose dimension is on the order of $1 \times 10^4 km^2$ and should not be confused with the value of the upper divergence over each cumulonimbus. As reported by McLean (1961), Fujita and Arnold (1963), and Matsumoto, Ninomiya and Nakagaki (1967), the magnitude of the divergence and/or the vertical velocity in a cumulonimbus is larger by one order of magnitude or more than the mean value evaluated in a whole storm area.

Another interesting feature of the upper level flow pattern is the appearance of strong winds along the northwest boundary of the storm area (see Figs. 3b and 4b). These strong winds are not only detected by using the clouds' movement but also observed by rawinsonde. As found in Fig. 9 of the next section, the wind speed at DAY exceeds 120 knots even at 500 mb. (The wind observation above 440 mb was missing at this station.) The vorticity field in the outflow layer was characterized by strong cyclonic vorticity to the north of the storm area. The magnitude of the relative vorticity is given by

$$\zeta = K_s V - \frac{\partial V}{\partial n} \qquad (2)$$

where V , K_s , and n are the wind speed, the curvature of the stream line and the distance normal to the stream line, respectively. The evaluation is made along the line $\widehat{AG}$ and $\widehat{ah}$ in Fig. 7a for the mature thunderstorm complex. To obtain the smoothed wind speed along these lines, the cloud movements used were within two 200 km wide zones centered on $\widehat{AG}$ and $\widehat{ah}$. The smoothed wind speed and calculated relative vorticity are presented in the lower part of Fig. 7a. The maximum of the cyclonic and anticyclonic vorticity is observed to the north and to the south of the northern boundary of the storm area, respectively, because the wind speed is largest along the northern boundary as mentioned.

The deformation field was analyzed in the outflow layer. It can be expressed as

$$a = \frac{\partial V}{\partial s} - V K_n \tag{3}$$

and

$$b = V K_s + \frac{\partial V}{\partial n} \tag{4}$$

where V, K_s, K_n, s and n are the wind speed, the curvature of the stream line, the curvature of the orthogonal line to the stream line, the distance along the stream line and the distance along the normal to the stream line, respectively. The magnitude of deformation is given by

$$d = a \cos 2\theta + b \sin 2\theta \tag{5}$$

or

$$|d| = \sqrt{a^2 + b^2} \tag{6}$$

where θ , the angle between the axis of dilatation and the orthogonal line, is calculated as

$$\theta = \frac{1}{2} \tan^{-1}\left(\frac{b}{a}\right) \tag{7}$$

The evaluation of deformation for the mature thunderstorm complex is made along the line $\widehat{KQ}$ in Fig. 7b while smoothed wind profiles along lines $\widehat{AG}$ and $\widehat{ai}$ in Fig. 7a are used. Results of the analysis show that the magnitude of deformation in the outflow layer is about $6 \times 10^{-5} sec^{-1}$, and the axis of dilatation is almost normal to the streamline.

It is noteworthy that the axis of dilatation is not parallel to the stream line but normal to it. It is also rather hard to assume an elongation towards the lateral direction for the isolated cumulonimbus from the growth of the anvil cloud. The remarkable lateral elongation or difluence in the upper layer would be the characteristic observed only over the group of thunderstorms.

In order to verify the results of this section, a comparison should be made with the results in the following section which were obtained by using rawinsonde data only. After 1700 CST as the darkness of the earth's shadow began to cover the eastern part of the area under consideration, it became too hard to evaluate the cloud movement. Therefore, only the comparison between the results of the analysis for 1600 CST by using the ATS cloud data and the results for 1800 CST by using rawinsonde data, is possible. The comparison seems, however, to be adequate because the life time of the mean outflow, whose horizontal scale is more than 500 km, would be sufficiently longer than the 2 hour time difference mentioned above.

4. Vertical Structure of the Outflow

Although the detail of the outflow and its growth could be studied by using high cloud movements as done in the previous section, the wind field in the layer under the outflow layer could not be studied by using ATS pictures. This was because the velocity of middle and low clouds can not be evaluated beneath dense high clouds. As a result, the vertical structure of the wind field in and under the outflow layer was analyzed by using the data of rawinsonde observations at 1800 CST.

A cloud distribution map at 1700 CST and the surface weather map at 1800 CST are shown in Fig. 8. Charts for the 250, 300, 500, and 700 mb surfaces at 1800 CST are shown in Fig. 9. As its spacing is more than 300 km, the mesoscale field can not be analyzed by using only the regular rawinsonde network. The large scale difluence

flow in the upper troposphere, however, was observed clearly around the storm area. The strongest difluence is observed on the 250-mb and 300-mb surfaces The difluence in the upper level is more clearly recognized in Fig. 10 by comparing the wind hodograph at the stations BUF and DIA which are situated on the north and south sides of the center of the convective storms. At 300 mb, the difference between the wind direction at BUF and DIA is as large as 60°. Fig. 10 also demonstrates the confluence in the lower troposphere between 650 and 750 mb. The confluence is strongest at 700 mb. Since the convective warm core exists in the layer between 600 and 400 mb, the wind field around the thunderstorm complex was characterized by the difluence above the warm core and the confluence below the warm core (for an example of a similar wind field, see Matsumoto and Ninomiya (1967)).

By using the wind observation at PIT, HTS, GSO, and DIA (see Fig. 8) the mean horizontal divergence over the quadrangle area enclosed by these stations is calculated as follows:

$$\overline{\mathrm{div}\, V} = \frac{1}{S} \oint V_n \, ds = \frac{1}{S} \sum_{i=1}^{4} V_{n_i} \cdot L_i \qquad (8)$$

where L_i and V_{n_i} are the length of the side and the wind component normal to L_i respectively. The dimension of the area, S, is about $10.1 \times 10^4 \mathrm{km}^2$. The vertical distribution of the mean horizontal divergence is presented in Fig. 11. The vertical velocity $\omega \left(= \frac{dp}{dt}\right)$ is, then, also calculated by using the continuity equation. The result is also shown in Fig. 11.

Upper divergence exists in a shallow layer between the 300 and 200-mb surface. The magnitude of the maximum divergence observed at 250 mb is as large as $7 \times 10^{-5} \mathrm{sec}^{-1}$. The layer of the horizontal convergence is observed below 700 mb and the mid-troposphere is characterized as the non-divergence layer. The large upward motion is, therefore, in the layer between 700 mb and 400 mb. Above 300 mb, the upward motion decreased rapidly and almost vanished at the 200-mb surface.

Analyses of rawinsonde data confirmed the conclusions about the vorticity field that were derived from the ATS pictures. It was shown in the previous section that the largest cloud velocity was found along the northwestern boundary of the storm area.

As seen in Fig. 9, the wind speed at DAY exceeded 120 knots even at the 500-mb surface. Since there were no wind observations at DAY above 440-mb, only the values of the geostrophic wind velocity above this height can be used. The maximum geostrophic wind speed of 130 knots was at 300-mb over DAY. The magnitude of the relative vorticity in the area to the northwest and to the southeast of the axis of the strongest wind are evaluated by using the geostrophic wind velocity at DAY and the observed wind velocities at FNT, PIA, PIT and HTS. The results of the evaluation are presented in Table 1. Since the jet stream is located along the northwestern boundary of the storm area, the upper tropospheric vorticity field in the vicinity of the storm area was characterized by the strong cyclonic vorticity to the northwest of the storm area and the strong anticyclonic vorticity over the storm area.

Analyses of the deformation field using the rawinsonde data verified the conclusion of the previous section obtained from the cloud velocity field. The analysis is made over the same area inwhich divergence and vertical velocity were evaluated. The magnitude of deformation d and the angle θ between the axis of dilatation and the y axis (here the calculation is made in the rectangular coordinates) are given as

$$d = A\cos 2\theta + B\sin 2\theta \tag{9}$$

and

$$\theta = \frac{1}{2}\tan^{-1}\frac{B}{A} \tag{10}$$

where

$$A = \frac{\partial u}{\partial x} - \frac{\partial v}{\partial y} \tag{11}$$

and

$$B = \frac{\partial v}{\partial x} + \frac{\partial u}{\partial y} \tag{12}$$

The angle between the axis of dilatation and the normal to the stream line, β is obtained from the wind direction and θ . As presented in Table 2, the magnitude of deformation in the outflow layer is as large as that of divergence and the axis of

Table 1. The magnitude of relative vorticity in the area to the northwest and to the southeast of the jetstream.

mb	Northwest	Southeast
200	$10 \times 10^{-5} sec^{-1}$	$-7 \times 10^{-5} sec^{-1}$
250	14	-8
300	18	-8
400	15	-8

Table 2. The magnitude of deformation, d, and the angle between the elongation axis and the normal to the stream line, θ

mb	$\|d\|$, $10^{-5} sec^{-1}$	θ deg
200	6	10
250	8	10
300	11	5
400	6	15

of dilatation is almost normal to the wind direction.

The conclusions obtained in the quantitative analyses of the upper wind field in this section coincide well with the results obtained using the high cloud movements in the previous section and support our confidence in the validity of those analyses.

5. The Warm Core in the Mid-Troposphere

The most remarkable feature in the thermal field over the storm area was a warm core in the mid-troposphere. As seen in Fig. 9, the difference between the temperature inside and outside the warm core is as great as 3C or more at the 500-mb surface. In addition, Fig. 9 shows high relative humidity within the core, itself. Fig. 12 represents the mean temperature sounding in the warm core which was obtained by averaging the rawinsonde observations at PIT, GSO, and HTS and clearly shows that the lapse rate in the layer between the 700-mb and the 400-mb surface is almost equal to the wet adiabatic lapse rate. Since the layer inside the warm core is characterized by high relative humidity, a wet-adiabatic lapse rate and strong mean upward motion (see Fig. 11), it is infered that the warm core was caused by the release of latent heat in the condensation process.

Because the thermal gradient of the large-scale field is so strong around the cut-off cold vortex (see Section 2) the thermal field of the warm core should be separated from the large-scale field. The temperature anomaly in the storm area is expressed by

$$\Delta T = \frac{1}{2}(T_{PIT} + T_{HTS}) - \frac{1}{2}(T_{DIA} + T_{DAY}) \qquad (13)$$

Since stations DAY and DIA are located just north and south, respectively, of the storm area, $\frac{1}{2}(T_{DIA} + T_{DAY})$ would give the temperature of the large-scale field. The vertical distribution of the temperature anomaly obtained by using equation (13) is presented in Fig. 13. The figure shows a temperature anomaly of 2C in the warm core between the 600-mb and the 400-mb surface. Above this warm core there is cold air

---

[3] An example of a similar temperature field was suggested by Fujita and Byers (1960) for a single huge cumulonimbus and another was analysed by Matsumoto and Ninomiya (1967) for mesoscale convective storms in wintertime. Yet another analogous situation is the thermal structure of the warm core of a tropical cyclone and the associated upper outflow (see Yanai 1968) even though there are differences between the wind field of a tropical cyclone and that of a severe storm.

as seen in the 300 and the 250-mb maps in Fig. 8. This cold air is a result of the overshooting of convective motions.

Because convective warming in the deep layer of the mid-troposphere increases the layer's thickness between the 700-mb and the 300-mb surfaces, there is local anomaly of the geopotential height of the isobaric surface in a warm core. The Laplacian of the geopotential height of the isobaric surface, $\nabla^2 \phi$ would be a good indication of the geopotential height anomaly because it expresses the curvature of the isobaric surface. The vertical distribution of $\nabla^2 \phi$ calculated over the same area on which the temperature anomaly was evaluated, is presented in Fig. 13. The figure shows that the maximum of the negative value, i.e., the maximum anomaly, was just above the warm core (c.f. Matsumoto, Ninomiya and Akiyama 1967) (for the relationship of the negative value of $\nabla^2 \phi$ to the upper divergence field, see Section 7).

As mentioned previously, the large-scale thermal gradient is strong to the south of the cut-off cold core. As the convective warm core is situated to the southeast of the cut-off cold air, the strongest thermal gradient appears to the northwest of the storm area and has a maximum value of 2C/100 km. Although the reverse temperature gradient in the southern part of the warm core is partly canceled out by the large-scale gradient, still a weak reverse thermal gradient can be seen in the 500-mb surface (Fig. 9).

Hodographs of the geostrophic wind are shown in Fig. 14 for the northside and the southside of the storm area. The northside hodograph was obtained by using geopotential height at DAY, HTS, and PIT and the southside hodograph was calculated by using observations at HTS, PIT and DIA. The figure shows that to the north of the warm core the geostrophic wind speed increases rapidly with height up to the 300 mb surface. Then it decreases with height due to the reverse thermal gradient which is caused by warm air over the cut-off cold air and the cold air over the storm area. To the south of the warm core, the speed of the geostrophic wind is almost unchanged, but its direction varies with height from southerly in the lower levels to westerly in the upper levels.

The results of the analysis show that the strong wind in the outflow layer along the northwest boundary of the cirrus sheet over the thunderstorms, the relatively weak wind to the south of the storms, and the difluence flow over the storm (see Fig. 14

and also 5b and 9) are caused by the characteristic thermal field around the storm area.

6. Thermodynamical Aspects in the Upper Outflow Layer and the Warm Core

Several analyses have been made to clarify the role of convective transfer of heat and moisture in the thermodynamical process of the atmosphere. In their budget analysis of a tropical storm Riehl and Malkus (1961) stressed the role of convective transfer (i. e., the hot tower hypothesis), while Matsumoto (1967) and Ninomiya (1968a, b) analyzed quantitatively the convective transfer in convective storms in wintertime.

In this section the role of the convective transfer of heat and moisture in the thermodynamical process in the upper outflow layer and the warm core will be clairfied by analyzing the continuity equation of water vapor and the thermodynamical equation for the mean motion using the rawinsonde observation data at 1800 CST. For the purpose of the analysis, convective terms should be introduced in these two equations. They are written as (Ninomiya 1968a)

$$\left[\overline{\frac{\partial q}{\partial t}} + \overline{\nabla \cdot V q} + \frac{\partial}{\partial p} \bar{\omega}\, \bar{q} \right] + \frac{\partial}{\partial p} \overline{\omega' q'} = - m^* \qquad (14)$$

and

$$c_p \left[\overline{\frac{\partial T}{\partial t}} + \overline{\nabla \cdot V T} + \frac{\partial}{\partial p} \bar{\omega}\, \bar{T} - \frac{R}{c_p} \frac{\bar{T}\bar{\omega}}{p} \right] + c_p \frac{\partial}{\partial p} \overline{\omega' T'} = L m^* \qquad (15)$$

where q is the mixing ratio of water vapor, m^* the condensation amount in the unit air mass, R the gas constant, c_p the specific heat of the air in a constant-pressure process, and L is the latent heat of vaporization. The bar $\overline{\ }$ and the prime $'$ in eqs. (14) and (15) denote the mean value in the area under consideration and the deviation from it, respectively. Since the deviation field is due to the sub-grid size convective motions, the terms $-\frac{1}{g} \overline{\omega' q'}$ and $-\frac{c_p}{g} \overline{\omega' T'}$ represent the vertical convective transfer of the water vapor and of the sensible heat, respectively. The mean upward velocity $\bar{\omega}$ is given as

$$\bar{\omega} = \nabla \cdot \int_{\mu}^{p_s} V \, dp + \frac{\partial p_s}{\partial t} \qquad (16)$$

where p_s indicates the surface pressure.

It is more convenient for the following discussion to rewrite the eqs. (14) and (15) as

$$\left(\frac{\overline{\delta}}{\delta t}\right)\overline{q} + \frac{\partial}{\partial p}\,\overline{\omega' q'} = -m^* \tag{17}$$

and

$$c_p\left(\frac{\overline{\delta_l}}{\delta t}\right)\overline{T} + c_p\,\frac{\partial}{\partial p}\,\overline{\omega' T'} = L\,m^* \tag{18}$$

where the net increment of the mixing ratio due to the mean motion $\left(\frac{\overline{\delta}}{\delta t}\right)\overline{q}$ and of the temperature $\left(\frac{\overline{\delta_l}}{\delta t}\right)\overline{T}$ are defined as

$$\left(\frac{\overline{\delta}}{\delta t}\right)\overline{q} = \frac{\overline{\partial q}}{\partial t} + \overline{\nabla\cdot \mathbf{V} q} + \frac{\partial}{\partial p}\,\overline{\omega}\,\overline{q} \tag{19}$$

and

$$\left(\frac{\overline{\delta_l}}{\delta t}\right)\overline{T} = \frac{\overline{\partial T}}{\partial t} + \overline{\nabla\cdot \mathbf{V} T} + \frac{\partial}{\partial p}\,\overline{\omega}\,\overline{T} - \frac{R}{c_p}\,\frac{\overline{\omega}\,\overline{T}}{p} \tag{20}$$

respectively.[4]

In the continuity equation of water vapor, eq. (14), only the terms in the brackets are evaluated by using the rawinsonde observation data, while both $\frac{\partial}{\partial p}\,\overline{\omega' q'}$ and m^*

---

[4] Instead of eqs. (17) and (18), or (15) and (16),

$$\frac{\overline{\partial q}}{\partial t} + \overline{\nabla\cdot \mathbf{V} q} + \frac{\partial}{\partial p}\,\overline{\omega}\,\overline{q} = -m^*$$

and

$$c_p\left[\frac{\overline{\partial T}}{\partial t} + \overline{\nabla\cdot \mathbf{V} T} + \frac{\partial}{\partial p}\,\overline{\omega}\,\overline{T} - \frac{R}{c_p}\,\frac{\overline{\omega}\,\overline{T}}{p}\right] = L\,m^*$$

are sometimes used for the mean field. It is not correct, however, in the convective area because the most important process in the distribution of heat energy, i.e., the convective transfer of heat energy, is left out.

could not be evaluated with rawinsonde data. A similar situation occurs in the thermodynamic equation, eq. (15), where $c_p \frac{\partial}{\partial p} \overline{\omega' T'}$ and m^* can not be evaluated with rawinsonde data, either. In order to evaluate separately the vertical convective transport of water vapor and heat, it is necessary, therefore, to know the vertical distribution of the amount of condensation. As we do not have the necessary information on the vertical distribution of m^*, the equation of total heat energy is used instead, which is obtained by multiplying eq. (14) by L and adding eq. (15) as

$$c_p \left[\frac{\partial \overline{T}}{\partial t} + \overline{\nabla \cdot V T} + \frac{\partial}{\partial p} \overline{\omega} \overline{T} - \frac{R}{c_p} \frac{\overline{\omega} \overline{T}}{p} \right]$$
$$+ L \left[\frac{\partial \overline{q}}{\partial t} + \overline{\nabla \cdot V q} + \frac{\partial}{\partial p} \overline{\omega} \overline{q} \right] + \frac{\partial}{\partial p} \left[c_p \overline{\omega' T'} + L \overline{\omega' q'} \right] = 0 \qquad (21)$$

or

$$c_p \left(\frac{\overline{\delta}}{\delta t} \right) \overline{T} + L \left(\frac{\overline{\delta}}{\delta t} \right) \overline{q} + \frac{\partial}{\partial p} \left[c_p \overline{\omega' T'} + L \overline{\omega' q'} \right] = 0 \qquad (22)$$

The convective term $\frac{\partial}{\partial p} \left[c_p \overline{\omega' T'} + L \overline{\omega' q'} \right]$ in eq. (21) or (22) can be evaluated as the residual term once the mean terms are evaluated by using the rawinsonde observation data. The evaluations are made in the quadrangle bounded by the four rawinsonde stations PIT, HTS, GSO and DIA. The mean horizontal divergence of water-vapor flux and sensible heat flux are calculated as

$$\overline{\nabla \cdot V q} = \frac{1}{S} \sum_{i=1}^{4} V_{n_i} q_i L_i$$

and

$$c_p \overline{\nabla \cdot V T} = c_p \frac{1}{S} \sum_{i=1}^{4} V_{n_i} T_i L_i$$

where L_i is the length of the side, V_{n_i} the wind component normal to L_i and q_i and T_i are the mean value of q and T along L_i respectively. The dimension of the quadrangle, S, is about $10.1 \times 10^4 \text{ km}^2$. The value of the mean vertical velocity $\overline{\omega}$ given by eq. (16) and the areal averaged values $\overline{T}$ and $\overline{q}$ are used to calculate $\frac{\partial}{\partial p} \overline{\omega} \overline{T}$, $\frac{R}{c_p} \frac{\overline{\omega} \overline{T}}{p}$ and $\frac{\partial}{\partial p} \overline{\omega} \overline{q}$. The terms involving local time

change in eq. (21) in the layer below 800 mb are evaluated by using the surface observation both in plain and mountainous areas and these terms in the layer above 800 mb are calculated by using the space-time transformation technique,

$$\frac{\partial}{\partial t} = -C\frac{\partial}{\partial s} \tag{23}$$

where C and S are the propagation velocity and direction of the system.

Thus the evaluated magnitude of each mean term in eq. (21) is integrated in each layer between two isobaric surfaces. The results[5] of the evaluation are presented in Figs. 15 and 16.

Once the vertical distribution of $\left[c_p \left(\frac{\overline{\delta_l}}{\delta t}\right)\overline{T} + L\left(\frac{\overline{\delta}}{\delta t}\right)\overline{q} \right]$ is obtained, the value of $-\frac{1}{g}\left(c_p\overline{\omega'T'} + L\overline{\omega'q'}\right)$ can be obtained at an arbitrary pressure surface by integrating $\left[c_p\left(\frac{\overline{\delta_l}}{\delta t}\right)\overline{T} + L\left(\frac{\overline{\delta}}{\delta t}\right)\overline{q}\right]$ from the top of the outflow layer to the pressure surface with the boundary condition that the convective transfer vanishes at the top of the outflow layer p_1 as

$$-\frac{1}{g}\left(c_p\overline{\omega'T'} + L\overline{\omega'q'}\right) = \frac{1}{g}\int_p^{p} \left[c_p\left(\frac{\overline{\delta_l}}{\delta t}\right)\overline{T} + L\left(\frac{\overline{\delta}}{\delta t}\right)\overline{q}\right] dp \tag{24}$$

The results are also presented in Fig. 16.

The most interesting features of the vertical distribution of $\left[c_p\left(\frac{\overline{\delta_l}}{\delta t}\right)\overline{T} + L\left(\frac{\overline{\delta}}{\delta t}\right)\overline{q}\right]$ are its large positive value in the upper troposphere and its negative value in the lower troposphere (c.f., Matsumoto 1968). Eq. (22) and Fig. 16 show that the net increment of the total heat energy in the upper outflow layer is balanced by the vertical convergence of the convective transfer of the heat energy. The results of the analysis show that the large amount of convective transfer of heat energy across the base of the outflow layer thermodynamically maintains the mean motion in the outflow layer.

---

[5] Since $\nabla\cdot V T_a + \frac{\partial}{\partial p}\omega T_a$ is zero for an arbitrary constant T_a, the value of the three dimensional flux divergence $\nabla\cdot V T + \frac{\partial}{\partial p}\omega T$ is equal to $\nabla\cdot V(T - T_a) + \frac{\partial}{\partial p}\omega(T - T_a)$. In Fig. 15, the values of $\overline{\nabla\cdot V(T-220)}$ and $\frac{\partial}{\partial p}\overline{\omega}(\overline{T}-220)$ are presented instead of the values of $\overline{\nabla\cdot V T}$ and $\frac{\partial}{\partial p}\overline{\omega}\,\overline{T}$ to simplify the discussion. The mean air temperature at the 200-mb surface is approximately 220 K.

Previously, it was mentioned that the net increment of the total heat energy appears in the outflow layer and that the large amount of heat energy is transported into the outflow layer by the convective motion. The following discussion would explain the physical meaning of the results of the heat energy budget analysis in the outflow layer.

The equation of total heat energy eq. (21) is expressed by using the equivalent potential temperature[6] $\theta_e = \pi (T + \frac{L}{C_p} q)$ where π indicates $(\frac{1000}{p})^{\kappa}$ and then integrating from the bottom of the outflow layer p_1 to the top of the layer p_2 ,

$$\frac{c_p}{g}\int_{p_1}^{p_2}\overline{\frac{\partial \theta_e}{\partial t}}\,dp + \frac{c_p}{g}\int_{p_1}^{p_2}\overline{\nabla\cdot V\theta_e}\,dp + \frac{c_p}{g}\overline{\theta_e}_2\overline{\omega}_2 + \frac{c_p}{g}\overline{(\theta_e'\omega')}_2 = 0 \qquad (25)$$

(Both the mean upward motion $\overline{\omega}$ and the convective transfer $\frac{c_p}{g}\overline{\theta_e'\omega'}$ vanish at the top of the outflow layer.) In order to simplify the discussion, eq. (25) is rewritten with the aid of eq. (23) and the continuity relation

$$\hat{\nabla}\cdot\hat{V}\,\Delta p + \overline{\omega}_2 = 0 \qquad (26)$$

as

$$\left[\frac{c_p}{g}(\hat{V}-C)\cdot\hat{\nabla}\theta_e\,\Delta p\right] + \left[\frac{c_p}{g}(\hat{\theta}_e - \overline{\theta}_{e_2})\,\hat{\nabla}\cdot\hat{V}\,\Delta p\right] + \frac{c_p}{g}\overline{(\theta_e'\omega')}_2 = 0 \qquad (27)$$

In eqs. (26) and (27), $\wedge$ indicates the vertical mean value in the outflow layer and Δp is defined as $p_2 - p_1$. Since the magnitude of the second term in eq. (27) is two or three times greater than that of the first term, the second term seems to be balanced mainly by the third term of eq. (27). The difference between $\hat{\theta}_e$, the mean equivalent potential temperature in the outflow layer,

---

[6] For the small value of the mixing ratio, the equivalent potential temperature $\theta_e = \pi T \exp(\frac{Lq}{C_p T})$ is written as $\theta_e = \pi T (1 + \frac{Lq}{C_p T})$.

and $\overline{\theta_{e_2}}$, the equivalent potential temperature at the base of the layer, is positive and its value is 5K in the area under consideration. Thus we have approximately 25 ly hour^{-1} for the second term since the mean divergence in the outflow layer is 5 x 10^{-5} sec^{-1}. In other words, the horizontal out-flux of equivalent potential temperature from the storm area associated with the horizontal mass divergence in the outflow layer is larger than the amount of the mean upward transfer of equivalent potential temperature across the base of the outflow layer because $\frac{\partial \theta_e}{\partial p}$ is negative in the layer. (The difference between $\hat{\theta}_e$ and $\bar{\theta}_{e_2}$, i.e. $\hat{\theta}_e - \bar{\theta}_{e_2}$ in eq. (27), is expressed as $\hat{\theta}_e - \bar{\theta}_{e_2} \cong \frac{1}{2}(\bar{\theta}_{e_1} + \bar{\theta}_{e_2}) - \bar{\theta}_{e_2} \cong -\frac{1}{2}\frac{\partial}{\partial p}\theta_e \Delta p$.) The difference between the horizontal outflow of total heat energy and the mean vertical transfer of the heat energy into the outflow laye. is supplied mainly by the convective transfer of the heat energy. Likewise it is easily shown that the convergence in the lower troposphere should increase the convective transfer of water vapor (Ninomiya 1968b).

At the end of this section, the value of the convective transfer in Figs. 15 and 16, which is evaluated as the residual term in the budget calculation, should be related to the characteristic thermodynamical quantities of the convective motion. As shown in the Appendix, we can express the convective transfer of total heat energy as

$$-\frac{1}{g}(c_p\overline{\omega'T'} + L\overline{\omega'q'}) \cong -\frac{1}{g}\sigma_c\,\omega_c\,(c_p\Delta_c T + L\Delta_c q) \cong -\frac{1}{g}\bar{\omega}\,(c_p\Delta_c T + L\Delta_c q) \tag{28}$$

where σ_c is the area ratio of the convective upward motion, ω_c the convective upward velocity, $\Delta_c T$ and $\Delta_c q$ are the convective excess temperature and excess mixing ratio, respectively. Although we do not have precise information about $\Delta_c T$ and $\Delta_c q$, 2K of the excess temperature and 2gm kg^{-1} of the excess mixing ratio have not been considered unusual (see for instance, Fujita and Byers 1960, Matsumoto, Ninomiya and Nakagaki 1967). As mentioned in section 4, the mean vertical velocity in the mid-troposphere is about 25 mb hour^{-1}. By using these values in eq. (28), the magnitude of the convective transfer of the heat energy is evaluated to be approximately

40 ly hour^{-1}. This value coincides rather well with the value of the convective transfer obtained from the budget calculation and indicates the validity of the budget calculation.

7. Dynamical Aspects of the Upper Divergence

In this section some dynamical aspects of the wind field of the large scale upper outflow will be analysed. Since the wind field in the upper outflow layer is characterized by strong divergence, it is appropriate to use the divergence equation instead of the momentum equation for discussing the dynamical mechanism of the outflow. The divergence equation relevant to the mean motion in the outflow layer is written as

$$\overline{\frac{\partial D}{\partial t}} + \overline{V\cdot\nabla D} + \bar{\omega}\,\overline{\frac{\partial D}{\partial p}} + \left(\frac{\partial \bar{\omega}}{\partial x}\frac{\partial \bar{u}}{\partial p} + \frac{\partial \bar{\omega}}{\partial y}\frac{\partial \bar{v}}{\partial p}\right) + \frac{1}{2}\left(\bar{D}^2 + \bar{A}^2 + \bar{B}^2 - \bar{\zeta}^2\right) - f\bar{\zeta} + \nabla^2\phi + \left[\overline{\omega'\frac{\partial D'}{\partial p}} + \frac{1}{2}\overline{D'^2}\right] = 0 \qquad (29)$$

where D is divergence, ζ is relative vorticity, and $A = \frac{\partial u}{\partial x} - \frac{\partial v}{\partial y}$ and $B = \frac{\partial v}{\partial x} + \frac{\partial u}{\partial y}$ are deformations (see Matsumoto, Ninomiya and Akiyama 1967). The bar —— and prime ' are used in the same way as in eqs. (14) and (15) in section 6. The convective term in eq. (29), to be precise, should be

$$\left[\overline{\omega'\frac{\partial D'}{\partial p}} + \left(\overline{\frac{\partial \omega'}{\partial x}\frac{\partial u'}{\partial p}} + \overline{\frac{\partial \omega'}{\partial y}\frac{\partial v'}{\partial p}}\right) + \frac{1}{2}\left(\overline{D}^2 + \overline{A}^2 + \overline{B}^2 - \overline{\zeta}^2\right)\right]$$

Although we do not have enough information on these correlation terms, it is inferred from the dynamical nature of convective motion that $\overline{\omega'\frac{\partial D'}{\partial p}}$ and $\overline{D'^2}$ are the most important.

Thus, in the divergence equation, eq. (29), $\left[\overline{\omega'\frac{\partial D'}{\partial p}} + \frac{1}{2}\overline{D'^2}\right]$ is introduced as the most important of the convective terms. The mean terms in eq. (29) are evaluated over the storm area by using rawinsonde observation at 1800 CST. (The time-space transformation technique given in eq. (23) was applied to the first term of eq. (29).) The estimated value of each mean term over the storm area is given in Table 3.

Table 3. The estimation of the divergence equation (unit = 10^{-8} sec^{-2})

	300 mb	250 mb
$\frac{\partial \overline{D}}{\partial t} + \overline{V} \cdot \nabla \overline{D}$	0.1	0.3
$\overline{\omega} \frac{\partial \overline{D}}{\partial p}$	0.3	0.0
$\frac{\partial \overline{\omega}}{\partial x} \frac{\partial \overline{v}}{\partial p} - \frac{\partial \overline{\omega}}{\partial y} \frac{\partial \overline{u}}{\partial p}$	0.1	0.0
$\frac{1}{2}(\overline{D}^2 + \overline{A}^2 + \overline{B}^2 - \overline{\zeta}^2) - f\overline{\zeta}$	0.6	0.8
$\nabla^2 \phi$	-1.9	-1.0

On the 250-mb surface, the surface of maximum divergence, the main terms of eq. (29) are $\nabla^2 \phi$, $\frac{\partial \overline{D}}{\partial t}$, $\overline{V} \cdot \nabla \overline{D}$ and $\left[\frac{1}{2}(\overline{D}^2 + \overline{A}^2 + \overline{B}^2 - \overline{\zeta}^2) - f\overline{\zeta}\right]$. Both the twisting terms and $\overline{\omega} \frac{\partial \overline{D}}{\partial p}$ are negligibly small on this surface. It should be emphasized that the large scale divergence in the outflow layer is due to the negative value of $\nabla^2 \phi$ which is caused by the convective warming in the midtroposphere.

The eddy terms in eq. (29) could not be evaluated directly by using rawinsonde observation and so were evaluated as the residual terms. The value of $\left[\overline{\omega' \frac{\partial D'}{\partial p}} + \frac{1}{2}\overline{D'^2}\right]$ was 0.1×10^{-8} sec^{-2}. This value is smaller than the value of $\nabla^2 \phi$ by one order of magnitude, and hence the role of the convective eddy terms seems to be less important at the 250-mb surface than on the surface of maximum $\nabla^2 \phi$, the 300-mb surface, where the role of the convective eddy terms seems to be significant because the estimated value of the eddy terms is 1×10^{-8} sec^{-2}, which is obtained by the residual calculations. This large value of the convective eddy terms on the 300-mb surface is the reason why the maximum divergence appears in a higher level than the level of the maximum of the negative $\nabla^2 \phi$.

The vertical distribution of the magnitude of the convective eddy terms, which is estimated in the residual calculation, is related to the dynamical property of the convective motion. As explained in the appendix, the convective eddy terms are written as

$$\frac{1}{2}\overline{D'^2} \cong \frac{1}{2}\sigma_c(D_c - \bar{D})\cdot(D_c - D_f) \cong \frac{1}{2}\bar{D}(D_c - D_f) \qquad (30)$$

and

$$\overline{\omega'\frac{\partial D'}{\partial p}} \cong \bar{\omega}\left(\frac{\partial D_c}{\partial p} - \frac{\partial D_f}{\partial p}\right) \qquad (31)$$

where D_c and D_f are the divergence in and out of the upward convective motion respectively. Although we do not have much information on the convective motion in higher levels, still some qualitative aspects of the eddy terms can be discussed. It can be inferred that ω_c is almost constant in the mid-troposphere because the mean vertical velocity $\bar{\omega} = \sigma_c \omega_c + \sigma_f \omega_f$ is almost constant and therefore $\bar{D}$, D_c and also $\frac{\partial D_c}{\partial p}$ will be almost zero. Above 400 mb, D_c increases with height up to the middle of the outflow layer. The difference between D_c and D_f on the other hand, becomes rapidly smaller with height due to lateral mixing. The mean vertical velocity $\bar{D}$ and also mean divergence $\bar{\omega}$ vanish at the top of the outflow layer. Therefore, the values of the convective eddy terms are small in the mid-troposphere and increase with height. The maximum will be somewhere in the lower part of the outflow layer and will vanish at the top of the outflow layer. Since ω_c and D_c are larger than $\bar{\omega}$ and $\bar{D}$ respectively, by one order of magnitude, eqs. (30) and (31) indicate that the maximum value of the convective eddy terms will be $10^{-8}\ \mathrm{sec}^{-2}$.

The convective eddy terms in the divergence equation, eq. (29), correspond to those in the momentum equation. For example, the considerably large magnitude of $\overline{\omega'\frac{\partial D'}{\partial p}}$ in eq. (29) suggests the strong vertical convective transfer of the horizontal momentum, which has been considered one of the important mechanisms of severe storm development (see Newton (1963), and Matsumoto and Nitta (1964)).

8. The Influence of the Convective Warming on the Mean Vertical Motion in the Storm Area

There were several ways to analyze the influence of the convective warming on the wind field. Manabe (1956), for example, analysed the change of the potential vorticity in the large scale field due to the released latent heat in the area of intense precipitation. Solving the ω – equation which included the terms of diabatic heating, Danard (1964) also showed the influence of the released latent heat on the large-scale wind field. He estimated the amount of diabatic heating by using the amount of condensation which was evaluated from the kinematically computed vertical velocity.

In the case presented here, the influence of the convective warming on the mean upward motion will be analysed by means of the ω – equation. When the vorticity equation and the thermodynamic equation are combined to eliminate the terms of time change of the geopotential and temperature, the familiar ω – equation is obtained,

$$\sigma \nabla^2 \bar{\omega} + f^2 \frac{\partial^2 \bar{\omega}}{\partial p^2} + \frac{R}{c_p} \frac{1}{p} \nabla^2 \left(\frac{\overline{\delta Q}}{\delta t} \right) + \left\{ \nabla^2 \left[V \cdot \nabla \left(\frac{\partial \phi}{\partial p} \right) \right] - f \frac{\partial}{\partial p} \left[V \cdot \nabla (f + \zeta) \right] \right\} = 0 \tag{32}$$

where σ is defined as $-\alpha \frac{\partial}{\partial p} \ln\theta$ and $\left(\frac{\overline{\delta Q}}{\delta t} \right)$ is defined as diabatic heating for the mean motion. The vertical motion caused by the third term and the last term are the thermally and dynamically forced upward motion, respectively.

In order to clarify the discussion, the thermally and the dynamically forced upward motion should be analysed separately. We will evaluate the thermally forced upward motion by using the ω – equation which involves the term of the diabatic heating,

$$\sigma \nabla^2 \bar{\omega} + f^2 \frac{\partial^2 \bar{\omega}}{\partial p^2} + \frac{R}{c_p} \frac{1}{p} \nabla^2 \left(\frac{\overline{\delta Q}}{\delta t} \right) = 0 \tag{33}$$

As already discussed in section 6, the diabatic heating for the mean motion $\left(\overline{\frac{\delta Q}{\delta t}}\right)$ is defined as

$$\left(\overline{\frac{\delta Q}{\delta t}}\right) \equiv c_p\left[\overline{\frac{\partial T}{\partial t}} + \overline{\vec{v}\cdot\nabla T} + \frac{\partial}{\partial p}\overline{\omega}\,\overline{T} - \frac{R}{c_p}\frac{1}{p}\overline{\omega T}\right] \tag{34}$$

$$= L\overline{m^*} - c_p\frac{\partial}{\partial p}\overline{\omega' T'}$$

where m^* means the amount of condensation per unit mass of the air. It is important to note that the diabatic heating for the mean motion is caused not only by the release of the latent heat Lm^* but also by the vertical convergence of the convective transfer of the sensible heat $c_p\frac{\partial}{\partial p}\overline{\omega' T'}$.

In order to evaluate the mean vertical velocity, the ω – equation, eq. (33) was rewritten in the form of simultaneous linear equations of $\overline{\omega}$ at each grid point, $\overline{\omega}_{i,j,k}$ by using the grid system shown in Fig. 17, where the area of the diabatic heating is indicated by stippling. The amount of the diabatic heating in each layer evaluated over the storm area in section 6 is adopted as the amount of diabatic heating in the heating area. Adiabatic motion is assumed outside this heating area. It was also assumed that the mean vertical velocity $\overline{\omega}$ vanishes at the lateral boundaries of the volume over which calculations are performed and on the 1000-mb and 100-mb surfaces. The values of $\overline{\omega}$ were obtained by solving the simultaneous equations. The horizontal divergence at each grid point was also calculated from the vertical velocity by using the continuity equation. The results for the center of the heating area are presented in Fig. 18. A comparison of these results (Fig. 18) with the mean vertical velocity and divergence obtained kinematically from the observed wind (Fig. 11) verifies the fact that the vertical velocity and the divergence obtained by solving eq. (33) show the characteristic features of the vertical distributions of the upward velocity and horizontal divergence in the storm area. The results indicate that the strong upward motion in the warm core and the remarkable high level divergence over the warm core are mainly induced and/or maintained by the convective warming.

Lastly we will study the dynamically forced vertical motion in the storm area by using the ω – equation for adiabatic motion

$$\sigma \nabla^2 \bar{\omega} + f^2 \frac{\partial^2 \bar{\omega}}{\partial p^2}$$

$$+ \left\{ \nabla^2 \left[V \cdot \nabla \left(\frac{\partial \phi}{\partial p} \right) \right] - f \frac{\partial}{\partial p} \left[V \cdot \nabla (f + \zeta) \right] \right\} = 0 \qquad (35)$$

It should be noted that the dynamically forced vertical motion is also influenced by the convective warming because the wind velocity and the vorticity, which are involved in the last term of eq. (35), have been modified in the vicinity of the warm core as shown in sections 4 and 5. In order to simplify the discussion, eq. (35) is rewritten by using the geostrophic wind approximation

$$\sigma \nabla^2 \bar{\omega} + f^2 \frac{\partial^2 \bar{\omega}}{\partial p^2} = f \frac{\partial V_g}{\partial p} \cdot \nabla (f + \zeta) \qquad (36)$$

In rewriting the equation, the terms which are insignificantly smaller than the term in the right side of eq. (36) are dropped. Since the left side of eq. (36) is negatively correlated with $\bar{\omega}$ itself, eq. (36) indicates that upward motion tends to occur in the region in which the thermal wind blows from the area of the maximum absolute vorticity to the area of the minimum vorticity and vice versa (Eliassen 1964).

It was shown in section 4 that the core of strong cyclonic vorticity is located to the northwest of the storm area and that the thermal wind is very strong along the northwestern boundary of the storm area. Therefore, the downward and upward motion are induced dynamically behind and ahead of the core of the cyclonic vorticity, respectively. This downward motion seems to intensify the dry area in the rear of the storm area. (see the 700-mb map in Fig. 9).

Although the core of anticyclonic vorticity was located within the storm area as mentioned in section 4, the dynamically forced vertical motion in the storm area was weak because the thermal wind was very weak in the storm area.

9. Concluding Remarks

On the upper level outflow and the midtropospheric warm core over the tornado-producing thunderstorms of April 23, 1968, a detailed synoptic and dynamic analysis

was made by using the conventional rawinsonde data combined with ATS III pictures obtained by the Tornado Watch Experiment of 1968.

The main results are summarized as follows:

1) No unusual mesoscale divergence in the upper level was found in the period prior to the development of the thunderstorms.

2) The velocity field of high-level clouds obtained by using the series of ATS pictures revealed the existence of mesoscale outflow from the developing thunderstorms. The magnitude of the mean divergence evaluated in the area whose horizontal dimension was on the order of $10 \times 10^4 km^2$ was about $10^{-4} sec^{-1}$.

3) As the number of the developing thunderstorms increased, the mesoscale outflow patterns modified the general flow and a large-scale outflow pattern was formed over the storm area.

4) A warm core was observed in the mid-troposphere beneath the large-scale outflow. The high humidity and also the strong upward motion in the warm core suggest that the warm core was due to the convective warming.

5) The wind field in the storm area was characterized by strong divergence and difluence above the warm core and also by strong convergence below the warm core.

6) The warm core intensified the thermal gradient to the northwest of the storm area. As explained by the thermal wind equation, the strong thermal gradient causes in part the strong vertical wind shear and strong wind observed to the northwest of the storm area.

7) Heat budget analysis indicates that the large amount of diabatic warming was necessary to maintain the mean motion in the outflow layer. This diabatic warming was due to the upward convective transfer of heat energy across the base of the outflow layer. This convective transfer was caused mainly by the convergence of water-vapor flux in the lower troposphere.

8) The dynamical aspects of the large-scale upper outflow was studied by using the divergence equation in the upper layer and also by using the ω -- equation with diabatic heating. The strong mean upward motion in the mid-troposphere and the strong mean divergence in the upper outflow layer were induced and maintained by the convective warming in the storm area.

APPENDIX

THE CONVECTIVE TRANSFER IN THE MEAN FIELD

The ratios of area of the core of upward convective motion and that of area outside of the core are denoted by σ_c and σ_f respectively. The values inside and outside of the core are indicated by the suffixes c and f . The areal mean is denoted by a bar— and the deviation from the mean by a prime ' . According to the definition we have

$$\sigma_c + \sigma_f = 1 \tag{A-1}$$

$$\bar{\omega} = \sigma_c \omega_c + \sigma_f \omega_f \tag{A-2}$$

and

$$\overline{a} = \sigma_c a_c + \sigma_f a_f \tag{A-3}$$

where ω is vertical velocity and a is an arbitrary scalar quantity. The total upward transfer of the quantity a is written as

$$\begin{aligned} \overline{\omega a} &= \sigma_c \omega_c a_c + \sigma_f \omega_f a_f \\ &= \bar{\omega}\bar{a} + \sigma_c \cdot \sigma_f (\omega_c - \omega_f)(a_c - a_f) \end{aligned} \tag{A-4}$$

or

$$\overline{\omega a} = \bar{\omega}\bar{a} + \sigma_f (\bar{\omega} - \omega_f)(a_c - a_f) \tag{A-5}$$

or

$$\overline{\omega a} = \bar{\omega}\bar{a} + \sigma_c (\omega_c - \bar{\omega})(a_c - a_f) \tag{A-6}$$

Therefore the eddy term is written as

$$\overline{\omega' a'} = \sigma_c (\omega_c - \bar{\omega})(a_c - a_f) \qquad \text{(A-7)}$$

(see also Yanai (1964), Matsumoto (1967) and Ninomiya (1968a)). As the ω_c is one order of magnitude or more larger than $\bar{\omega}$ and as the mean upward motion is mainly due to the convective motion, eq. (A-7) is roughly

$$\overline{\omega' a'} \cong \sigma_c \cdot \omega_c (a_c - a_f) \cong \bar{\omega} (a_c - a_f) \qquad \text{(A-8)}$$

REFERENCES

Danard, M.B., 1964: On the influence of released latent heat on cyclone development. J. Appl. Meteor. 3, 27-37.

Eliassen, A., 1964: Motions of Intermediate Scale: Fronts and Cyclones. Advances in Earth Science, The M.I.T. Press, Cambridge, Mass., 111-138.

Fawbush, E. J., R. C. Miller and L. G. Starret, 1951: An empirical method of forecasting tornado development. Bull. Amer. Meteor. Soc., 32, 1-9.

Fujita, T., 1963: Analytical mesometeorology. Meteor. Monographs., 5, No. 27, 77-128.

_____, and J. Arnold, 1963: Preliminary result of analysis of the cumulonimbus cloud of April 21, 1961. SMRP Research Paper #16, University of Chicago.

_____, and H. Byers, 1960: Model of a hail cloud as revealed by photogrammetric analysis. Tech. Rep. No. 3, University of Chicago, 9 pp.

_____, and D. L. Bradbury, 1969: Determination of mass outflow from a thunderstorm complex using ATS III pictures. Proc. 6th Conf. on Severe Local Storms, Amer. Meteor. Soc., 38-43.

Manabe, S., 1956: On the contribution of heat released by condensation to the change in pressure pattern. J. Meteor. Soc. Japan, 34, 308-320.

Matsumoto, S., 1967: Budget analysis on the sea effect snow observed along the Japan Sea coastal area. J. Meteor. Soc. Japan, 45, 53-63.

_____, 1968: Smaller scale disturbance in the temperature field around a decaying typhoon with special emphasis on the severe precipitation. J. Meteor. Soc. Japan, 46, 483-495.

_____ and K. Ninomiya, 1967: On the mesoscale warm core above the condensation level related to convective activities under the influence of dome shaped cold air. J. Meteor. Soc. Japan, 45, 306-314.

_____and_____, 1969: On the role of convective momentum exchange upon the mesoscale gravity wave. J. Meteor. Soc. Japan, 47, 75-85.

Matsumoto, S., K. Ninomiya and T. Akiyama, 1967: A synoptic and dynamic study on the three dimensional structure of mesoscale disturbances observed in the vicinity of a cold vortex center. J. Meteor. Soc. Japan, 45, 64-82.

Matsumoto, S., K. Ninomiya and K. Nakagaki, 1967: Measurement of the upward velocity and excess temperature in cumulus convection by means of dropsonde observation. J. Meteor. Soc. Japan, 45, 490-492.

McLean, G. S., 1961: Observation of severe convective activity in a squall line. Bull. Amer. Meteor. Soc., 42, 252-264.

Newton, C. W., 1963: Dynamics of severe convective storms. Meteor. Monographs, 5, No. 27, 33-58.

_____, 1967: Severe Convective Storms. Advances in Geophysics, Vol. 12, Academic Press, New York, 257-308.

Ninomiya, K., 1968a: Heat and water budget over the Japan Sea and the Japan Islands in winter season. J. Meteor. Soc. Japan, 46, 343-372.

_____, 1968b: Cumulus group activity over the Japan Sea in wintertime in relation to the water convergence in subcloud layer. J. Meteor. Soc. Japan, 46, 373-388.

Riehl, H. and J. Malkus, 1961: Some aspects of hurricane Daisy 1958. Tellus, 13, 181-213.

U. S. Weather Bureau, Staff Members of National Severe Storms Project, 1963: Environmental and thunderstorm structures as shown by National Severe Storms Project observations in spring 1960 and 1961. Mon. Wea. Rev., 91, 271-292.

Yanai, M., 1964: Formation of tropical cyclones. Rev. Geophys., 2, 367-414.

_____, 1968: Evolution of a tropical disturbance in the Caribbean Sea region. J. Meteor. Soc. Japan, 46, 86-109.

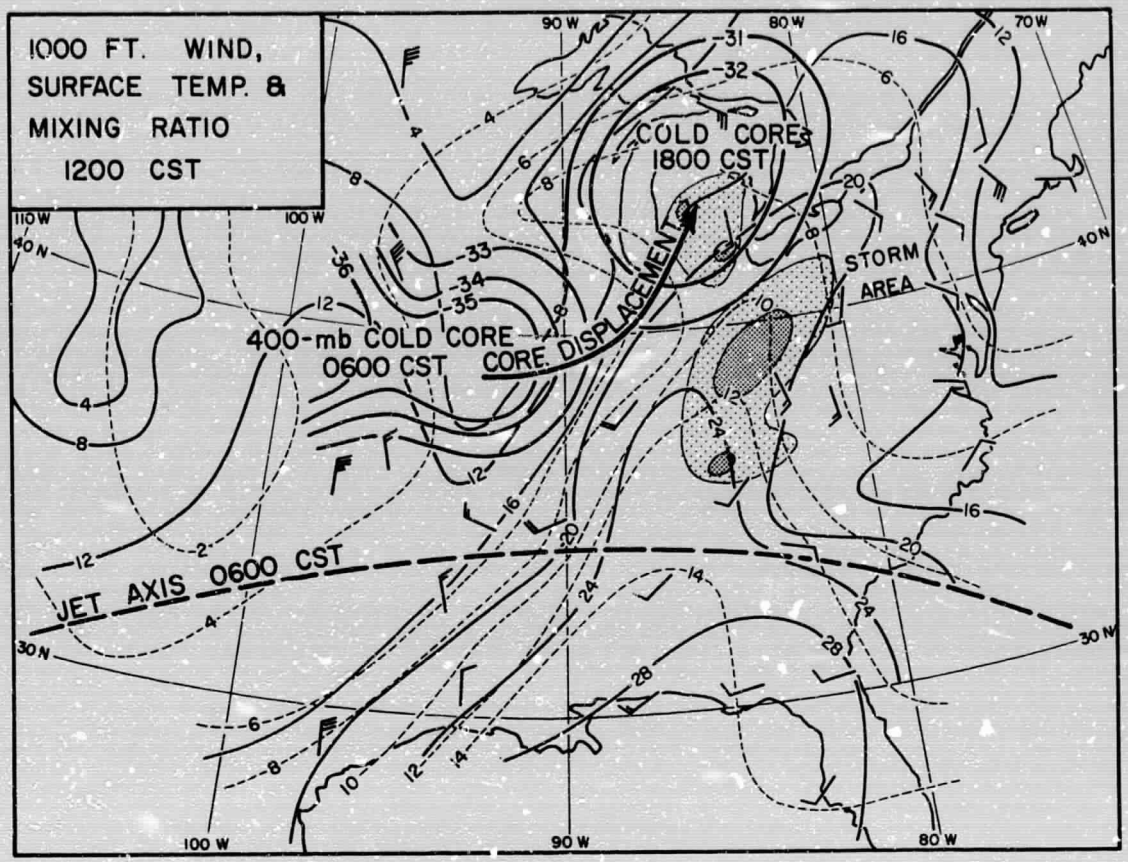

Fig. 1. Surface temperature (C, thin line), mixing ratio (gm. kg^{-1}, thin dashed line) and 1,000-ft winds at 1200 CST, 23 April 1968. The storm (tornado and hail) areas reported between 1200 CST and 1500 CST are indicated by the stipple. The movement of the cut-off cold core is also shown in this figure. The isotherms at 400 mb are drawn with thick solid lines.

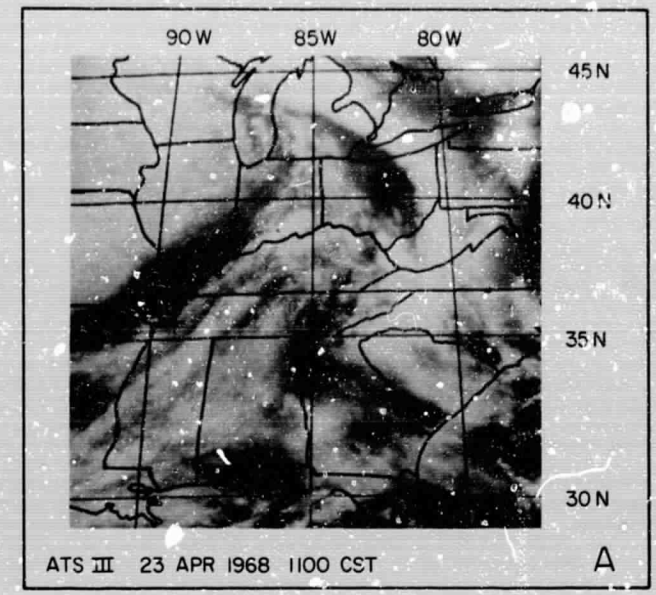

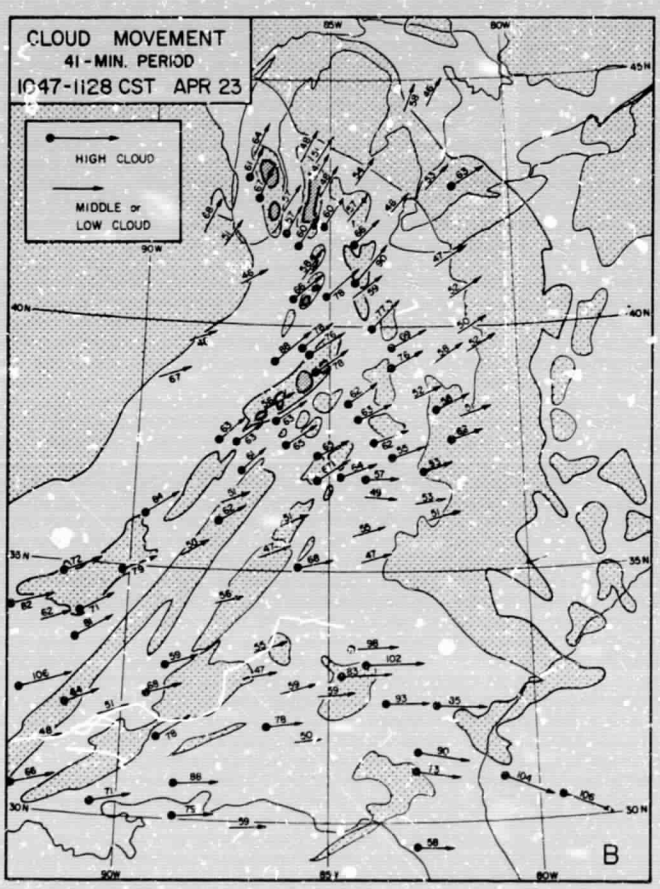

Fig. 2(A). A digitized ATS III picture at 1100 CST, April 23, 1968.

Fig. 2(B). The velocity field of clouds for the initial stage of the thunderstorm complex. The clouds' movements are obtained for a 41-min period from 1047 to 1128 CST. The figures indicate the wind speed (knot). The distribution of clouds (area of thin stipples) and radar echoes (area of dense stipples) is for 1100 CST.

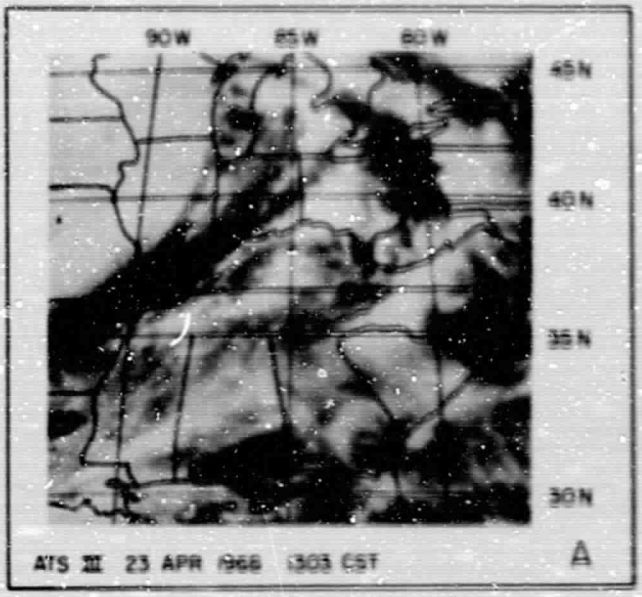

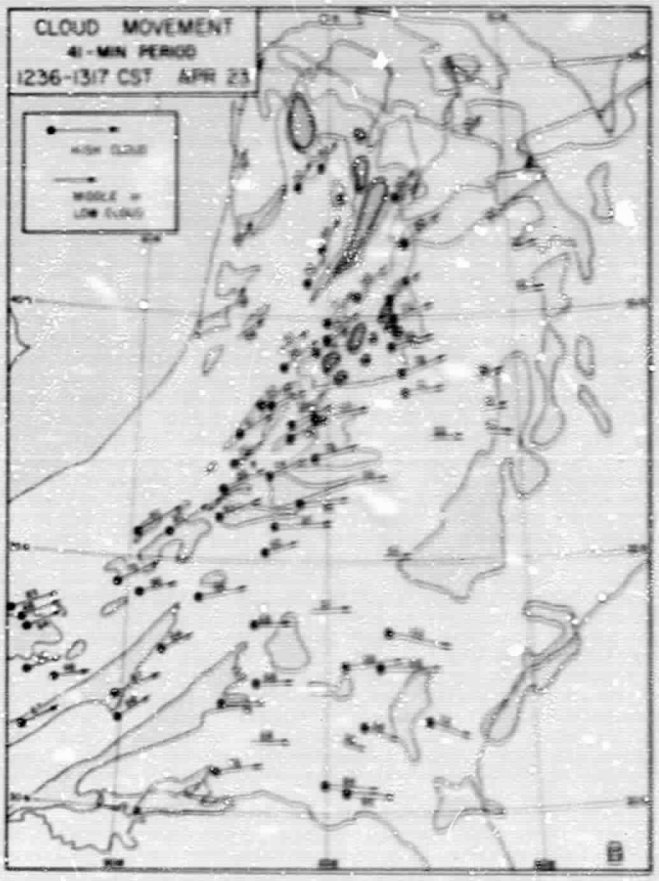

Fig. 30A). A digitized ATS III picture at 1304 CST, April 23, 1968.

Fig. 30B). The velocity field of clouds for the growing stage of the thunderstorm complex. The clouds' movements are obtained for a 41-min period from 1236 to 1317 CST. The distribution of clouds and radar echoes is for 1304 CST.

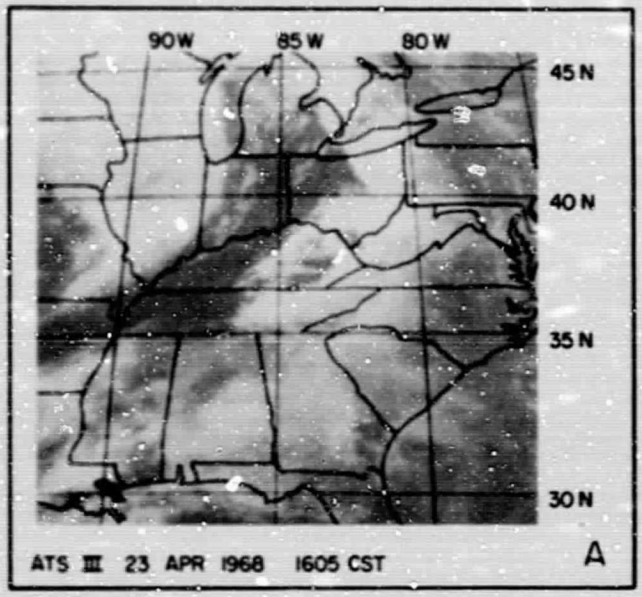

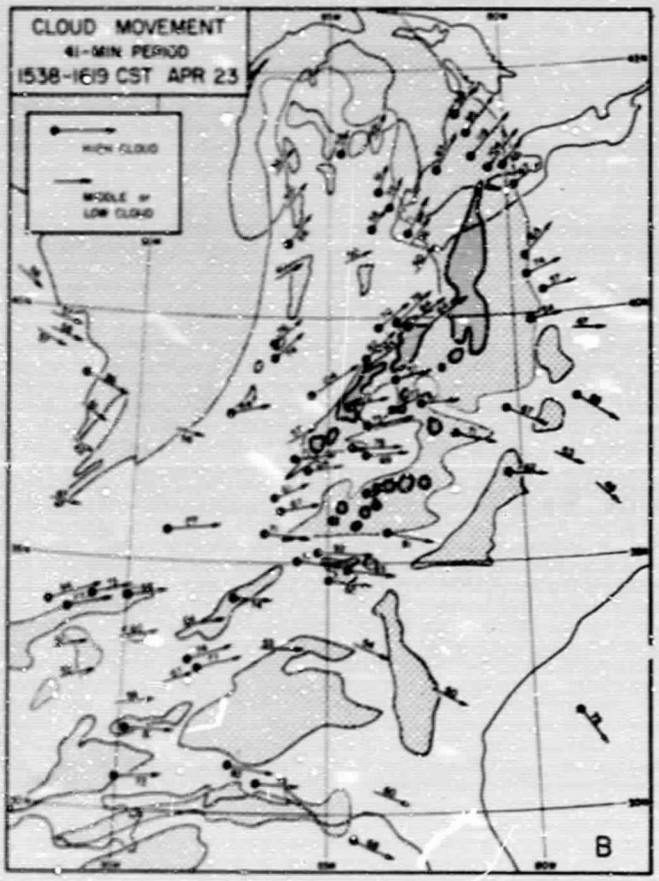

Fig. 4(A). A digitized ATS III picture at 1605 CST, April 23, 1968.

Fig. 4(B). The velocity field of clouds for the mature stage of the thunderstorm complex. The clouds' movements are obtained for a 41-min period from 1538 to 1619 CST. The distribution of clouds and radar echoes is for 1605 CST.

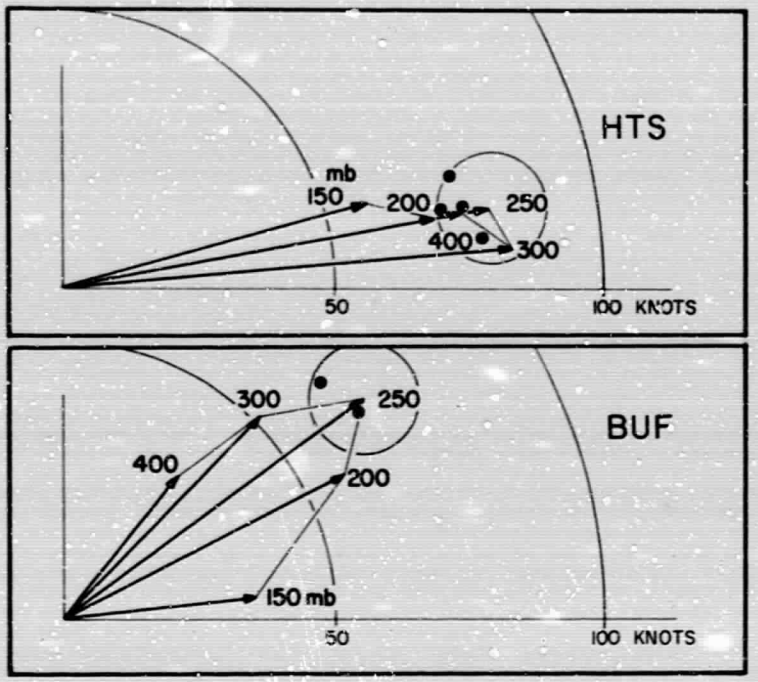

Fig. 5. The comparison between wind speed and velocity of high clouds in the neighborhood of the radiosonde station, HTS and BUF.

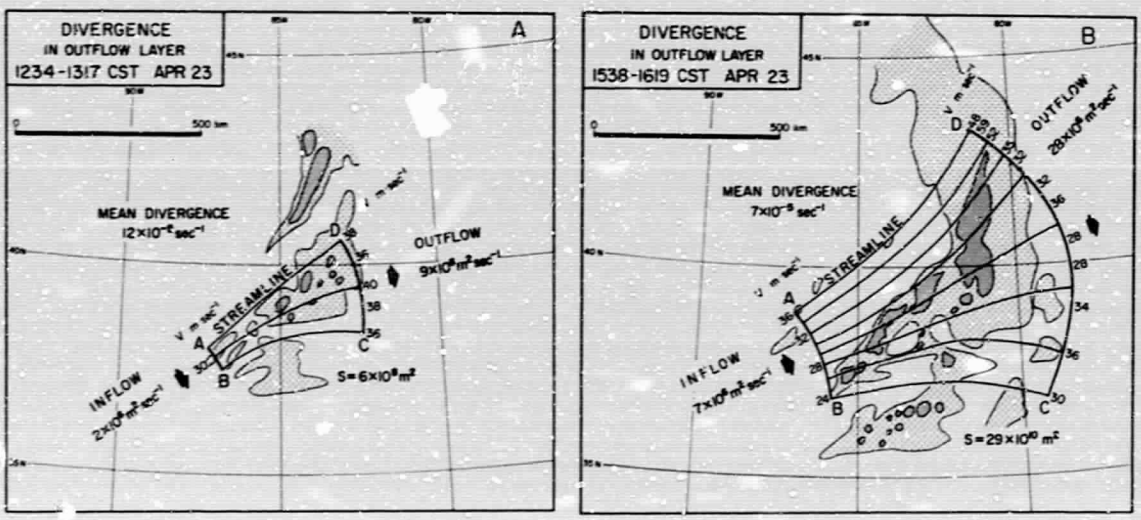

Fig. 6(A). Divergence in the outflow layer of the thunderstorm complex in the growing stage. Calculation is made by using the high clouds' movements for a 41-min period from 1236 to 1317 CST.

Fig. 6(B). Divergence in the outflow layer of the mature thunderstorm complex. Calculation is made by using the high clouds' movements for a 41-min period from 1538 to 1619.

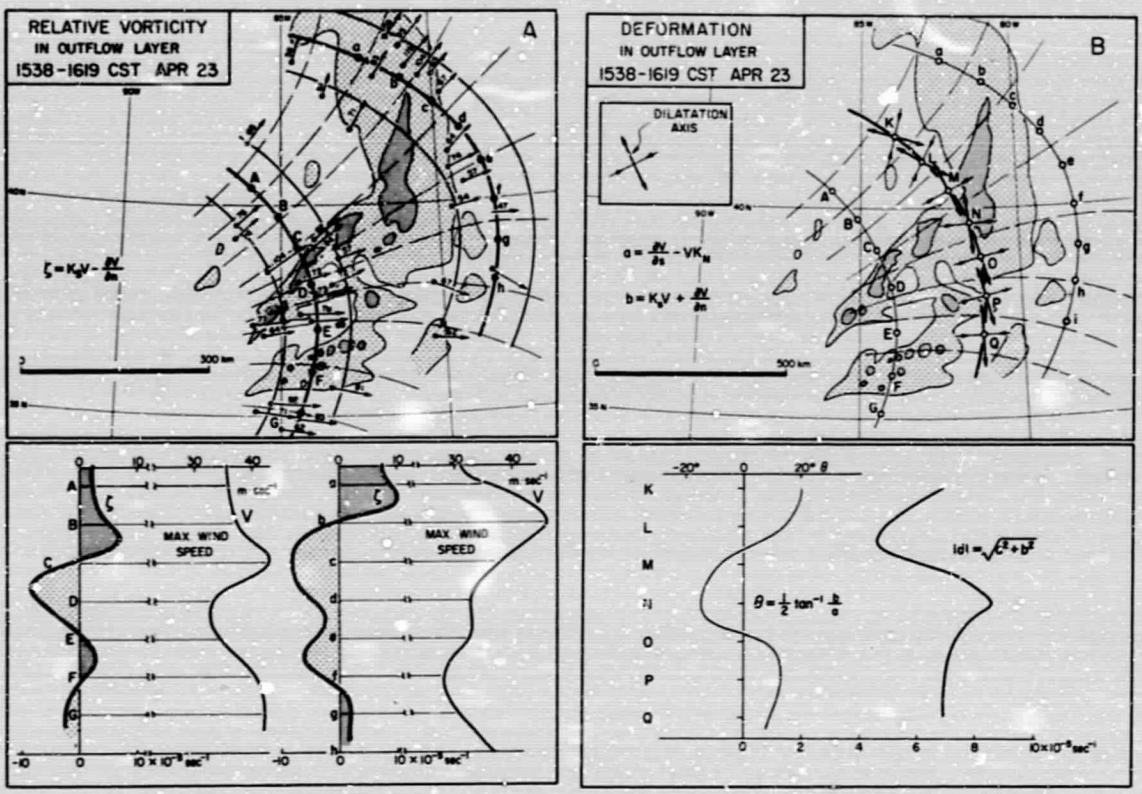

Fig. 7(A). Relative vorticity calculated along the line $\widehat{AG}$ and the line $\widehat{ah}$ by using the high clouds' movements for a 41-min period from 1538 to 1619 CST.

Fig. 7(B). The deformation field in the outflow layer evaluated along the line $\widehat{KP}$ by using the high clouds' movements for a 41-min period from 1538 to 1619 CST.

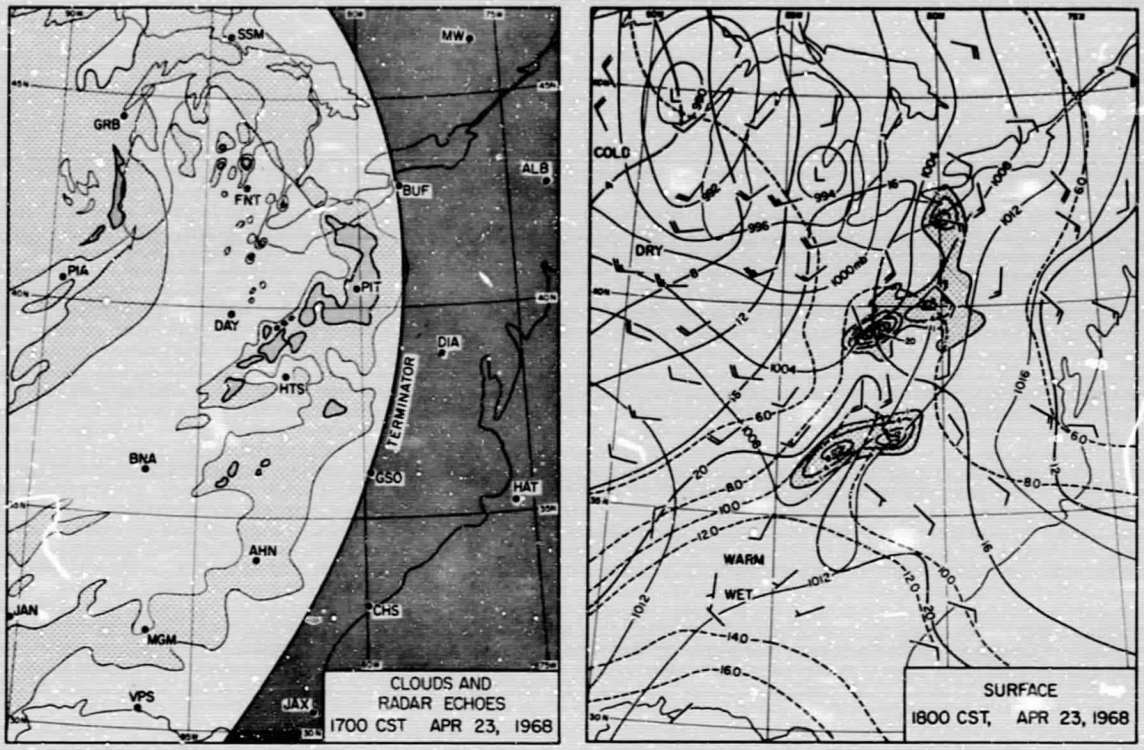

Fig. 8. Left: Distributions of clouds (indicated with thin stipples) and radar echoes (indicated with dense stipples) at 1700 CST, April 23, 1968. Right: The surfacw weather map at 1800 CST. April 23, 1968. Isobars, isotherms and isolines of mixing ratio are indicated by thin solid, solid and dashed lines, respectively. The isolines of the hourly precipitation amount (mm hour^{-1}) ending at 1800 CST are shown by the heavy solid lines.

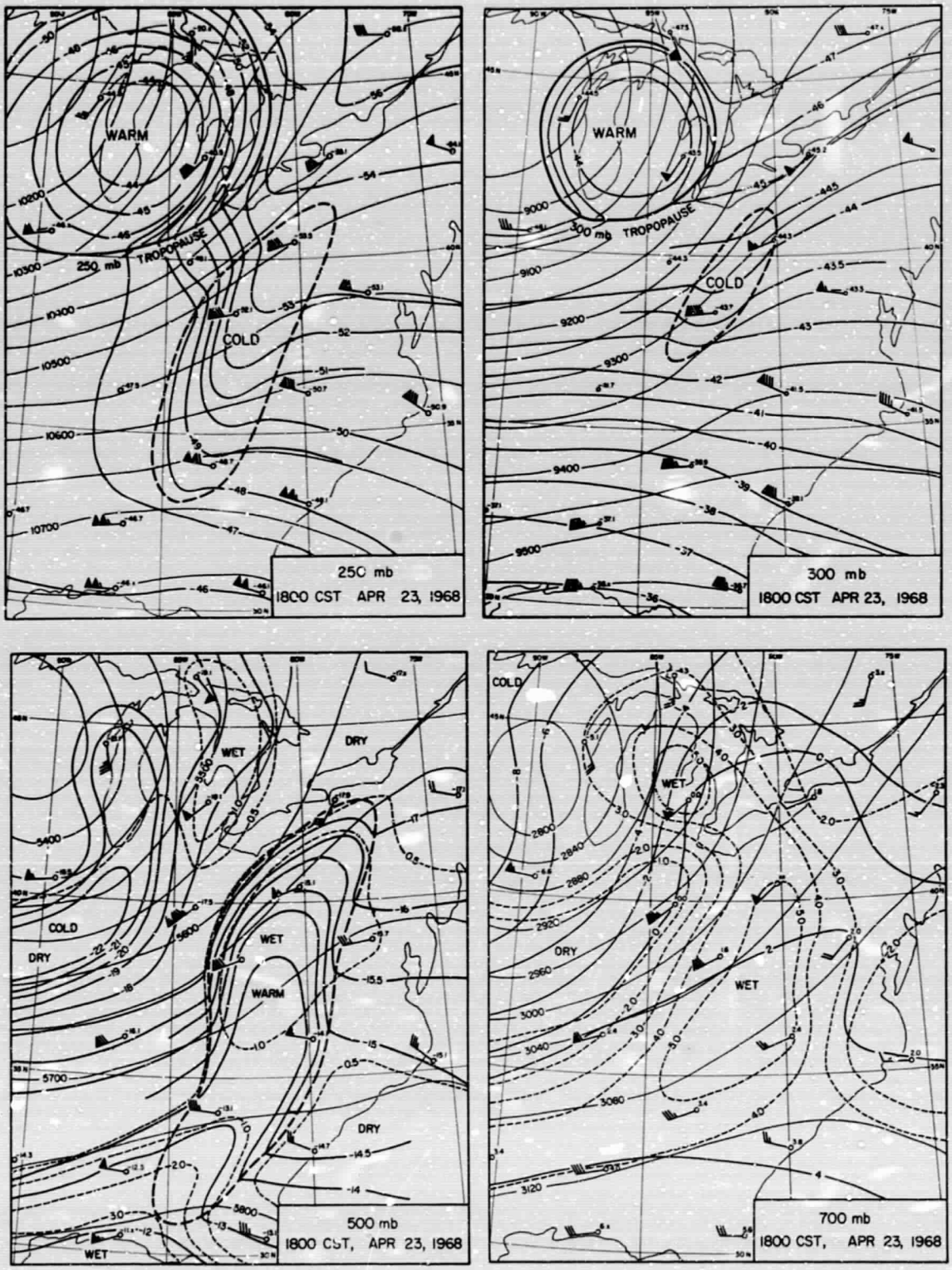

Fig. 9. 250, 300, 500 and 700 mb charts at 1800 CST, April 23, 1968. Height contours, isotherms and isolines of mixing are indicated by thin solid, solid and dashed line, respectively.

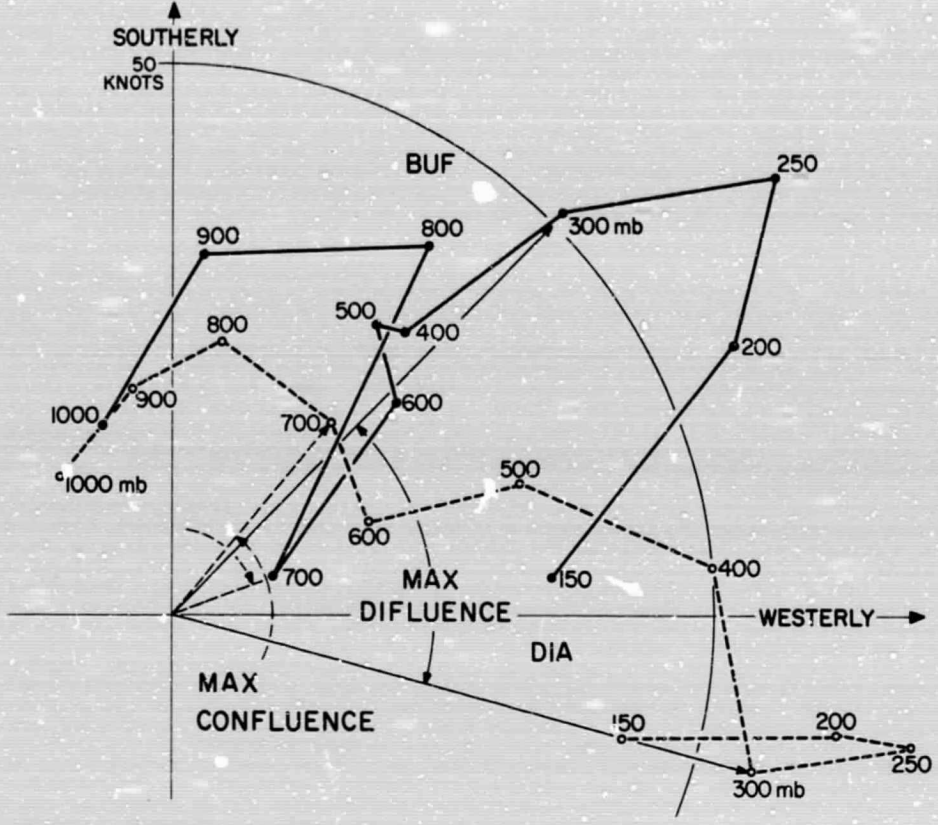

Fig. 10. Wind hodographs at BUF and DIA for 1800 CST, April 23. BUF and DIA were situated to the north and to the south of the storm area at the time. Note that the maximum difluence is at the 300-mb surface and the maximum confluence is at the 700-mb surface.

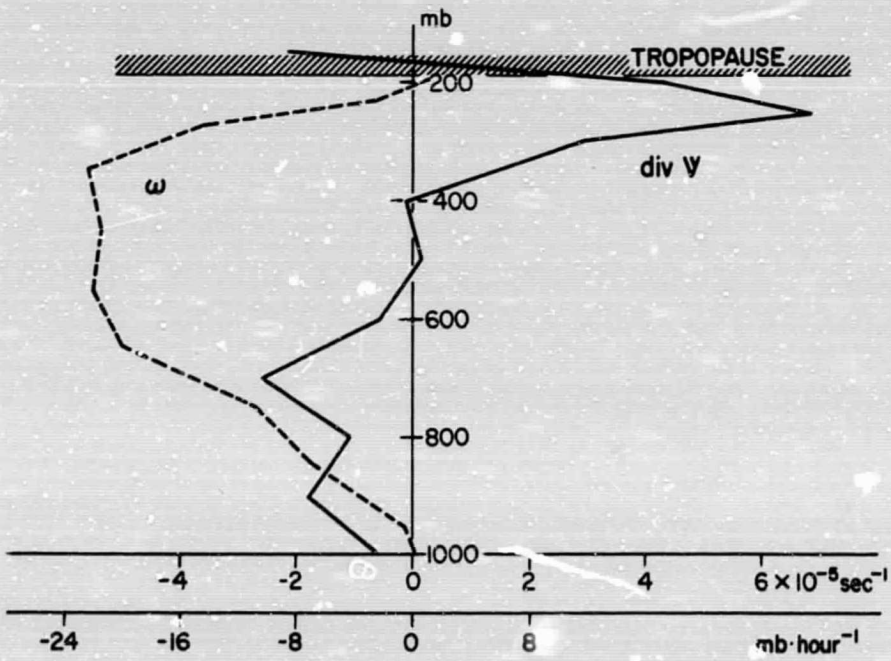

Fig. 11. Vertical distribution of the horizontal divergence and the vertical velocity calculated by using the upper wind data at PIT, HTS, GSO, and DIA for 1800 CST, April 23.

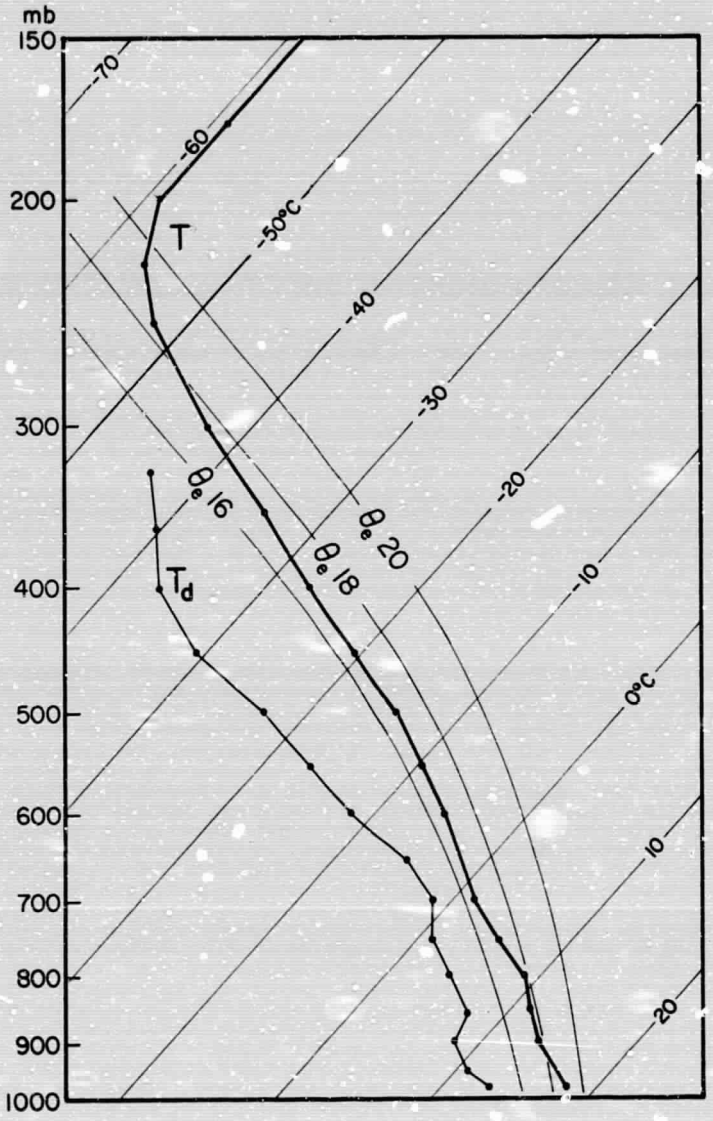

Fig. 12. The mean sounding in the warm core obtained by averaging the radiosonde observations at PIT, GSO, and HTS for 1800 CST.

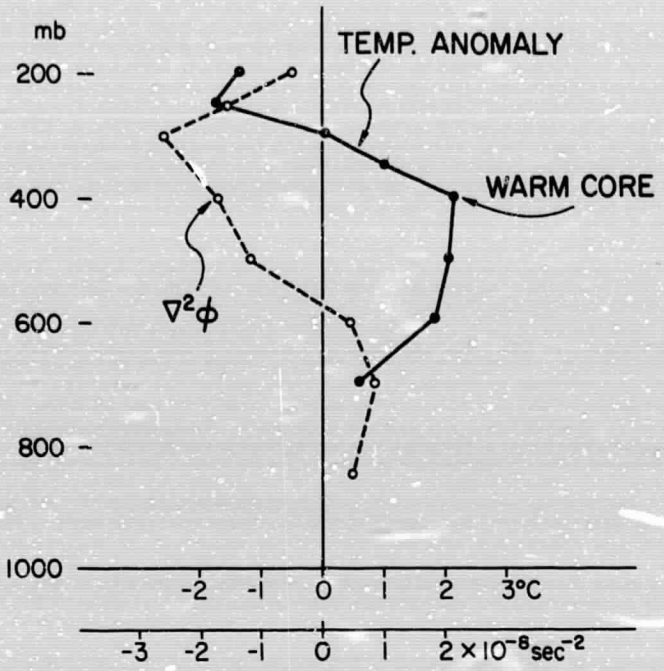

Fig. 13. Vertical distributions of the temperature anomaly in the warm core and $\nabla^2\phi$ calculated in the area of thunderstorm complex.

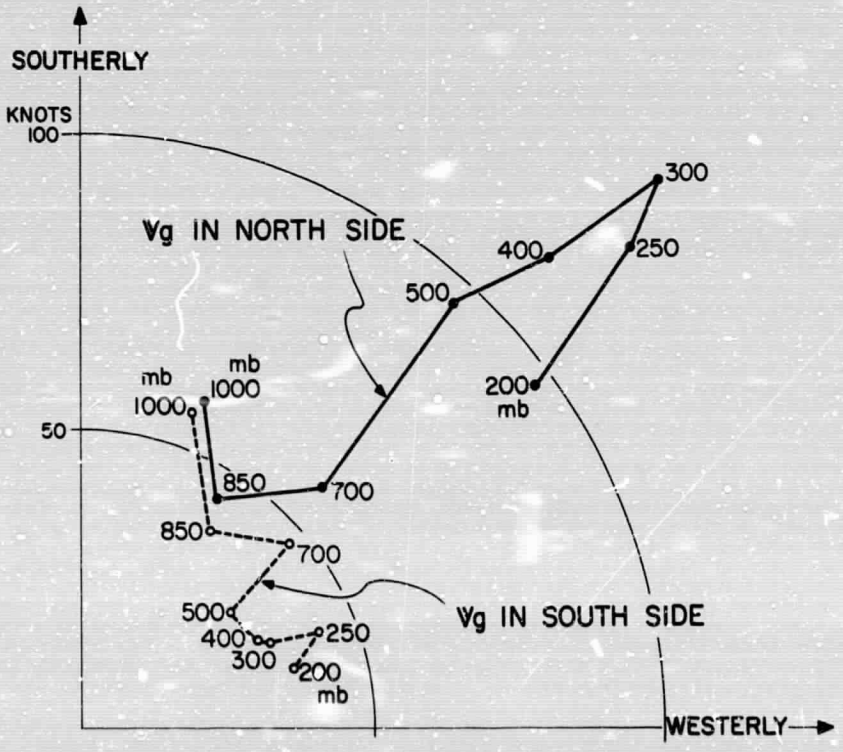

Fig. 14. Hodographs of the geostrophic wind in the north and the south side of the storm area.

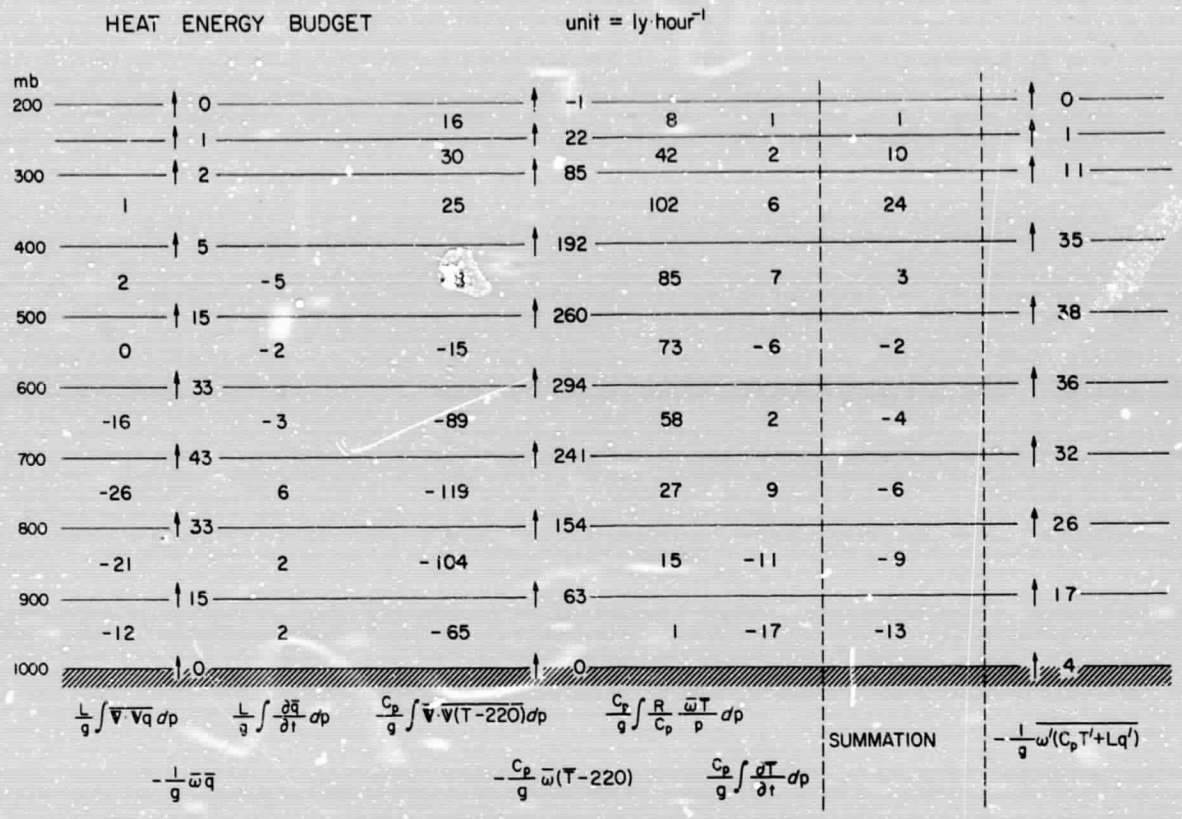

Fig. 15. Total heat energy budget over the mature thunderstorm complex.

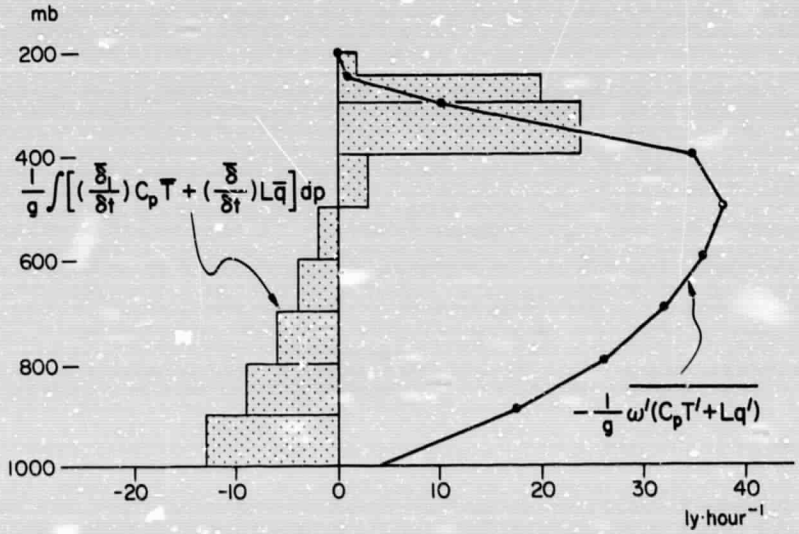

Fig. 16. The net increment of the toal heat energy for the mean motion in each layer over the mature thunderstorm complex $\frac{1}{g}\int\left[c_p\left(\overline{\frac{\delta_1}{\delta t}}\right)\bar{T}+L\left(\overline{\frac{\delta}{\delta t}}\right)\bar{q}\right]dp$

$$=\frac{1}{g}\int\left\{c_p\left[\frac{\overline{\partial T}}{\partial t}+\overline{\nabla\cdot V T}+\frac{\partial}{\partial p}\bar{\omega}\bar{T}-\frac{R}{c}\frac{\bar{\omega}\bar{T}}{p}\right]+L\left[\frac{\overline{\partial q}}{\partial t}+\overline{\nabla\cdot Vq}+\frac{\partial}{\partial p}\bar{\omega}\bar{q}\right]\right\}dp$$

and the convective transfer of total heat energy $\frac{1}{g}\overline{\omega'(c_pT'+Lq')}$

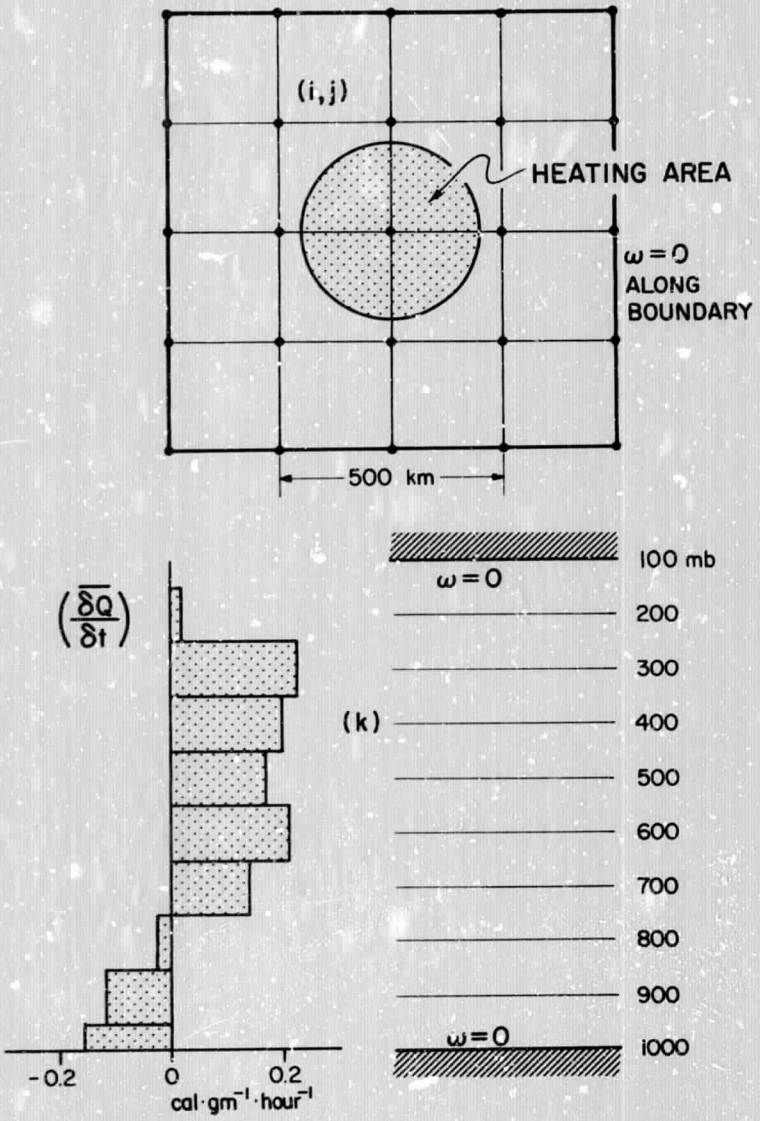

Fig. 17. The grid system used for solving eq. (34) and the vertical distribution of diabatic heating $\left(\frac{\overline{\delta Q}}{\delta t}\right)$ in the storm area.

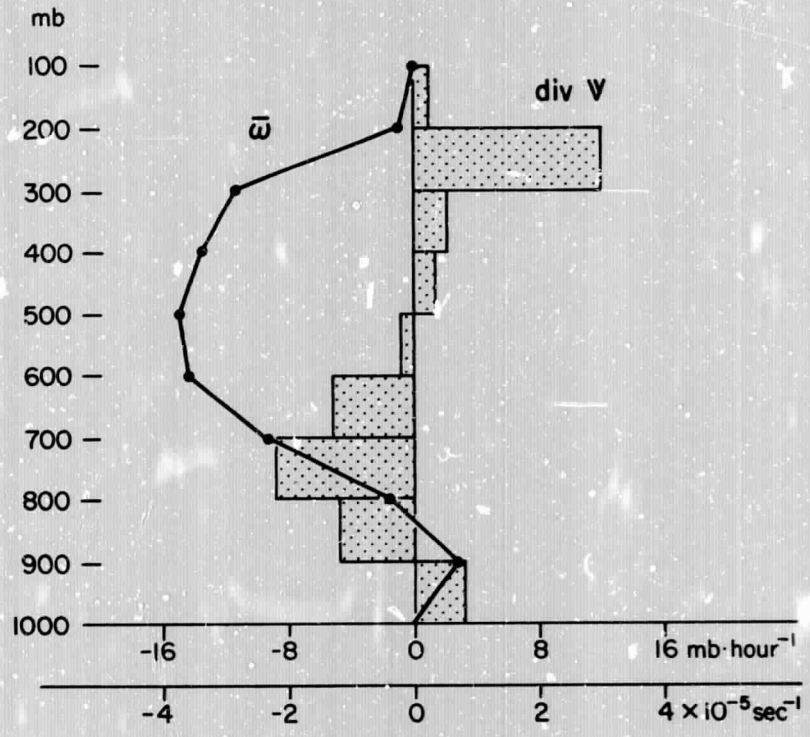

Fig. 18. The mean vertical motion and mean horizontal divergence forced thermally due to convective warming.

MESOMETEOROLOGY PROJECT - - - RESEARCH PAPERS

(Continued from front cover)

42.* A Study of Factors Contributing to Dissipation of Energy in a Developing Cumulonimbus - Rodger A. Brown and Tetsuya Fujita

43. A Program for Computer Gridding of Satellite Photographs for Mesoscale Research - William D. Bonner

44. Comparison of Grassland Surface Temperatures Measured by TIROS VII and Airborne Radiometers under Clear Sky and Cirriform Cloud Conditions - Ronald M. Reap

45. Death Valley Temperature Analysis Utilizing Nimbus I Infrared Data and Ground-Based Measurements - Ronald M. Reap and Tetsuya Fujita

46. On the "Thunderstorm-High Controversy" - Rodger A. Brown

47. Application of Precise Fujita Method on Nimbus I Photo Gridding - Lt. Cmd. Ruben Nasta

48. A Proposed Method of Estimating Cloud-top Temperature, Cloud Cover, and Emissivity and Whiteness of Clouds from Short- and Long-wave Radiation Data Obtained by TIROS Scanning Radiometers - T. Fujita and H. Grandoso

49. Aerial Survey of the Palm Sunday Tornadoes of April 11, 1965 - Tetsuya Fujita

50. Early Stage of Tornado Development as Revealed by Satellite Photographs - Tetsuya Fujita

51. Features and Motions of Radar Echoes on Palm Sunday, 1965 - D. L. Bradbury and T. Fujita

52. Stability and Differential Advection Associated with Tornado Development - Tetsuya Fujita and Dorothy L. Bradbury

53. Estimated Wind Speeds of the Palm Sunday Tornadoes - Tetsuya Fujita

54. On the Determination of Exchange Coefficients: Part II - Rotating and Nonrotating Convective Currents - Rodger A. Brown

55. Satellite Meteorological Study of Evaporation and Cloud Formation over the Western Pacific under the Influence of the Winter Monsoon - K. Tsuchiya and T. Fujita

56. A Proposed Mechanism of Snowstorm Mesojet over Japan under the Influence of the Winter Monsoon - T. Fujita and K. Tsuchiya

57. Some Effects of Lake Michigan upon Squall Lines and Summertime Convection - Walter A. Lyons

58. Angular Dependence of Reflection from Stratiform Clouds as Measured by TIROS IV Scanning Radiometers - A. Rabbe

59. Use of Wet-beam Doppler Winds in the Determination of the Vertical Velocity of Raindrops inside Hurricane Rainbands - T. Fujita, P. Black and A. Loesch

60. A Model of Typhoons Accompanied by Inner and Outer Rainbands - Tetsuya Fujita, Tatsuo Izawa, Kazuo Watanabe and Ichiro Imai

61. Three-Dimensional Growth Characteristics of an Orographic Thunderstorm System - Rodger A. Brown

62. Split of a Thunderstorm into Anticyclonic and Cyclonic Storms and their Motion as Determined from Numerical Model Experiments - Tetsuya Fujita and Hector Grandoso

63. Preliminary Investigation of Peripheral Subsidence Associated with Hurricane Outflow - Ronald M. Reap

64. The Time Change of Cloud Features in Hurricane Anna, 1961, from the Easterly Wave Stage to Hurricane Dissipation - James E. Arnold

65. Easterly Wave Activity over Africa and in the Atlantic with a Note on the Intertropical Convergence Zone during Early July 1961 - James E. Arnold

66. Mesoscale Motions in Oceanic Stratus as Revealed by Satellite Data - Walter A. Lyons and Tetsuya Fujita

67. Mesoscale Aspects of Orographic Influences on Flow and Precipitation Patterns - Tetsuya Fujita

68. A Mesometeorological Study of a Subtropical Mesocyclone -Hidetoshi Arakawa, Kazuo Watanabe, Kiyoshi Tsuchiya and Tetsuya Fujita

69. Determination of Tornado Wind Speed from Characteristic Ground Marks - Tetsuya Fujita, Dorothy L. Bradbury and Peter G. Black

70. Computation of Height and Velocity of Clouds from Dual, Whole-Sky, Time-Lapse Picture Sequences - Dorothy L. Bradbury and Tetsuya Fujita

71. A Study of Mesoscale Cloud Motions Computed from ATS-I and Terrestrial Photographs - Tetsuya Fujita, Dorothy L. Bradbury, Clifford Murino and Louis Hull

72. Aerial Measurement of Radiation Temperatures over Mt. Fuji and Tokyo Areas and Their Application to the Determination of Ground- and Water-Surface Temperatures - Tetsuya Fujita, Gisela Baralt and Kiyoshi Tsuchiya

73. Angular Dependence of Reflected Solar Radiation from Sahara Measured by TIROS VII in a Torquing Maneuver - Rene Mendez.

74. The Control of Summertime Cumuli and Thunderstorms by Lake Michigan During Non-Lake Breeze Conditions - Walter A. Lyons and John W. Wilson

75. Heavy Snow in the Chicago Area as Revealed by Satellite Pictures - James Bunting and Donna Lamb

76. A Model of Typhoons with Outflow and Subsidence Layers - Tatsuo Izawa

* out of print

(continued on outside back cover)

MESOMETEOROLOGY PROJECT - - - RESEARCH PAPERS

(Continued from inside back cover)

77. Yaw Corrections for Accurate Gridding of Nimbus HRIR Data - Roland A. Madden

78. Formation and Structure of Equatorial Anticyclones Caused by Large-Scale Cross Equatorial Flows Determined by ATS-I Photographs - Tetsuya T. Fujita and Kazuo Watanabe and Tatsuo Izawa

79. Determination of Mass Outflow From a Thunderstorm Complex Using ATS III Pictures - T. T. Fujita and D. L. Bradbury

80. Development of a Dry Line as Shown by ATS Cloud Photography and Verified by Radar and Conventional Aerological Data - Dorothy L. Bradbury